ROYAL SOCIETY
OF CHEMISTRY

CRITICAL REVIEW

Check for updates

Grazing incidence and grazing exit X-ray fluorescence: principles, techniques, and applications for thin film and nanostructure analysis

Yves Kayser, [iD] *[ab] Markus Krämer[c] and Philipp Hönicke [iD] *[bd]

In various technological fields, different nanomaterials are being used to push toward ever smaller and more complex structures. Different X-ray based methods can be extremely helpful to develop, analyze and improve such materials. Combining element sensitivity with lateral in-depth resolution, grazing incidence X-ray fluorescence (GIXRF) is a perfect candidate for this task. GIXRF represents an extension of standard X-ray fluorescence analysis (XRF) and total reflection XRF, and its utility has been demonstrated in a number of synchrotron studies over the years. Especially with improvements in X-ray sources and X-ray optics, GIXRF has become accessible to laboratory setups as well. Based on the principle of reciprocity, grazing emission – or gazing exit X-ray fluorescence (GEXRF) was postulated and proven to work in a similar way as GIXRF, with different advantages and disadvantages due to the inverse geometry. However, with their comparably more complex analysis procedures GIXRF and GEXRF methodologies are not yet widespread in research and industry. Thus, this review aims to give a comprehensive overview on the physical principle, technical requirements and recent applications in research and industry of these versatile nanoscale characterization methods.

1 Introduction

Grazing Incidence X-ray Fluorescence (GIXRF) and Grazing Emission X-ray Fluorescence (GEXRF) techniques are specialized methodologies within the broader field of X-ray Fluorescence (XRF) spectrometry. XRF, a well-established technique for bulk elemental analysis, typically involves the excitation of a sample with X-rays and the subsequent detection of characteristic fluorescent X-rays emitted by its constituent elements. In contrast to conventional XRF, where the excitation angles are relatively large (typically in the range of 30° to 60°), the excitation geometry for GIXRF is employing grazing incident angles near the angle for total external reflection. At angles below this material and photon energy dependent critical angle of total external reflection, the incident X-ray radiation is nearly fully reflected, when considering microscopically and macroscopically flat sample surfaces, *i.e.*, surface roughness comparable or smaller than the X-ray wavelength propagation at a grazing angle and no change in surface slope within the x-beam

propagation path, resulting in lowest penetration of the substrate, high excitation probability at the surface and low spectral background contributions. In total-reflection XRF (TXRF),[1,2] one takes advantage of this phenomenon to achieve lowest detection limits for ultra-sensitive element-sensitive contamination control on flat surfaces.

However, in GIXRF, unlike in TXRF, the angle of incidence is varied in a range around the critical angle to manipulate the in-depth excitation conditions and thereby obtain depth dependent fluorescence emission. At incidence angles below the critical angle for total external reflection, nearly all of the radiation is reflected at the sample surface and only a small fraction penetrates the sample near the surface. For incidence angles in the vicinity of and above the critical angle, the radiation is no longer completely reflected at the surface and an angle-dependent fraction penetrates deeper into the sample. The average penetration depths for GIXRF varies in the range of a few nm and several hundred nm up to several μm, depending on the excitation energy used, the angle of incidence and the sample material.

GIXRF also takes advantage of another phenomenon that occurs when an X-ray beam is reflected at a flat interface. In the case of total external reflection of a monochromatic parallel X-ray beam at a very flat interface, an X-ray standing wave field (XSW) is generated by interference between the incident and reflected beams above this interface. It is characterized by an

aMax Planck Institute for Chemical Energy Conversion, Stiftstrasse 34-36, Mülheim an der Ruhr, 45470, Germany. E-mail: yves.kayser@cec.mpg.de

bPhysikalisch-Technische Bundesanstalt (PTB), Abbestr. 2-12, 10587 Berlin, Germany. E-mail: philipp.hoenicke@ptb.de

cAXO DRESDEN GmbH, Gasanstaltstr. 8b, 01237 Dresden, Germany

dHelmholtz-Zentrum Berlin (HZB), Hahn-Meitner-Platz 1, 14109 Berlin, Germany. E-mail: philipp.hoenicke@ptb.de

alternating sequence of intensity maxima (anti node) and minima (node) and modifies the depth dependent intensity of the evanescent field even below the boundary layer. By varying the angle of incidence, these intensity modulations can be exploited in the standing wave field:[3–5] appropriate excitation conditions can be used, for example, to enhance the excitation of thin layers on the surface or even buried layers by shifting the wave field so that the intensity is maximal within the structure under investigation. In this way, the intensity of the fluorescence radiation produced is varied as a function of depth.

Due to the strong dependence of the vertical intensity distribution on the angle of incidence and photon energy, the standing wave field can be used very well as a nanoscale sensor to probe the in-depth distribution of elements of interest. An early application of this technique was the determination of arsenic ion implantation profiles in silicon. In the following years, several early applications of the GIXRF technique followed for ion implantation depth profiling and thin film stack characterization. For a more detailed summary of the early years, the reader is referred to the older review papers.[6,7]

In the same time period, Becker et al.[8] introduced GEXRF based on the principle of microscopic reversibility. It states that excitation and detection can also be considered in reverse. Thus, GEXRF can be introduced based on the geometry of GIXRF but by exchanging and inverting the paths for excitation and detection: the excitation is now similar to general XRF at rather large incident angles far above the critical angle but the detection of the fluorescence radiation is realized at very shallow angles. Thus, also in GEXRF the probed depth changes with the detection angle. A comparable interference pattern to the X-ray standing wave field in GIXRF can arise in GEXRF by interference of different possible detection paths. These serve as the nanoscale in-depth sensor in GEXRF.

Due to these features, both techniques are highly suitable for depth profiling applications in the surface near region providing sensitivities for in-depth changes in the nanometer regime. As a consequence of the reversed geometry, GIXRF and GEXRF have different advantages if compared to one another. However, for both techniques the depth-dependent information about the sample under test can only be derived indirectly employing forward-calculation based approaches. In the following, we provide a more detailed insight into the underlying theories of both techniques, provide different calculation examples and provide summaries of recent application in different areas for both techniques. This review completes the series of past reviews on GIXRF[6,9] and GEXRF,[10] as well as the work provided by Klockenkaemper and von Bohlen[7] and focuses mainly on the latest application examples, which were published after the publication of these previous works.

2 Grazing incidence X-ray fluorescence analysis

2.1 Theory of GIXRF

As in conventional XRF, the physical description of GIXRF experimental data is described by the Sherman equation.[11] It

allows the observed fluorescence emission under specific experimental conditions to be quantitatively correlated with the depth-dependent composition of the sample. In conventional XRF or TXRF applications, the Sherman equation is usually used to determine only the composition of the sample, or more precisely, the masses per unit area of the elements present. In GIXRF, however, dimensional information can also be obtained due to the profound changes in excitation conditions as the angle of incidence is changed. The Sherman equation for GIXRF can be written as

$$\frac{4\pi \sin\theta_i}{\Omega(\theta_i)}\frac{F(\theta_i, E_0)}{\Phi_0(E_0)\varepsilon_{E_f}} = W_j\rho Q\mathrm{d}z \cdot \sum_z P(z)\cdot I_{\mathrm{XSW}}(\theta_i, z)\cdot\exp\left[-\rho\mu_{E_f}z\right]$$

(1)

Here, the observed count rate $F(\theta_i, E_0)$ of the fluorescence line of interest at an incident angle θ_i and incident photon energy E_0 must be normalized with respect to the effective solid angle of detection $\Omega(\theta_i)/4\pi$, the incident photon flux $\Phi_0(E_0)$ and the detection efficiency ε_{Ef} of the detector used for the observed fluorescence line energy. The weight fraction W_j of the element of interest within the sample matrix, its density ρ and the fluorescence production cross section Q for the fluorescence line of interest combine for a scaling factor to match the calculated fluorescence intensity with the normalized experimental data. The depth dependent model for the distribution of the element of interest $P(z)$, the relative intensity factor $I_{\mathrm{XSW}}(\theta_i, z)$ for the X-ray standing wave at an angle of incidence θ_i and a depth z, and a self-attenuation correction factor for the fluorescence line of interest on its way out of the sample to the detector are calculated at each depth using the sample matrix mass attenuation factor for the fluorescence line energy before a numerical integration is performed to obtain the integral fluorescence emission at a given angle of incidence.

For depth profiling applications, an optimization algorithm is usually employed to automatically determine optimal values for the depth distribution of the element of interest within the sample matrix by comparing the theoretically calculated fluorescence emission at different incident angles (right side of eqn (1)) with the normalized experimental data (left side of eqn (1)). In reference-free GIXRF, where the employed instrumentation is physically calibrated,[12,13] all relevant parameters of the instrumentation used are known. If this is the case, the depth integral of the derived depth profile provides the total mass deposition or mass per unit area of the element of interest within the sample matrix. If not all of these parameters are known absolutely, only qualitative depth profiles can be derived. However, upon proper calibration employing well-known samples, such an instrument can also be enabled to derive quantitative results.[14]

In any case, the effective solid angle of detection, which results from the interplay between the field of view of the fluorescence detectors, the sample size, and the incident angle-dependent projection of the spatial intensity distribution of the incident beam, is of great importance as it strongly modifies the observed angular fluorescence emission and must therefore be taken into account. The effective solid angle or geometric

This journal is © The Royal Society of Chemistry 2025

J. Anal. At. Spectrom., 2025, **40**, 3368–3393 | **3369**

function is highly instrument specific, as the actual beam properties and detector geometry are critical parameters. Several publications[3,15–19] deal with this issue and should be considered when trying to approach this problem for any GIXRF instrument.

The other crucial parameter for the required forward-calculation modeling is of course the ability to calculate the angle and depth dependent X-ray standing wave intensity distribution $I_{XSW}(\theta_i, z)$. This in turn depends on the sample properties. Of course, the optical properties of the sample, which depend on the depth dependent composition, also determine the sample reflectivity for a given photon energy and angle of incidence. Since the XSW is a result of interference between incident and reflected waves, the dependence on optical properties is obvious. Consequently, the XSW calculation should be included in the forward-calculation and provided with the relevant sample properties. If the element of interest is present at a very low concentration, this may be negligible in special cases. For the calculation of standing wave fields for GIXRF experiments, the recursive algorithm[20] is usually used. DeBoer and colleagues[21] provided the first comprehensive physical description of GIXRF, allowing forward-calculation based modeling of GIXRF experimental data. Several different implementations for the calculation of the X-ray standing wave field exist[17,22–25] as a result of numerous research groups working with the technique in recent years. Some of these programs also provide tools for modeling experimental GIXRF datasets.

Due to the complementary nature of the analytical information provided by GIXRF and the dimensional information provided by X-ray reflectometry (XRR), a combined analysis of GIXRF and XRR data is also feasible, and often required, to obtain reliable depth profiling results.[23,26,27] This was already identified as a promising approach to improve GIXRF reliability by de Boer et al.[5] in the mid-1990s. However, this combined methodology has not really been used until about 2005. Since then, several research groups have taken up the idea and successfully applied it for in-depth characterizations of mostly nanolayered systems.[13,25,28–37] A special case here is the GIXRF-XRR based analysis of multilayers, where the XSW occurring around the Bragg reflection peaks of the multilayer is used to probe the in-depth material distributions either inside the multilayer[38–42] or on top of it.[43] Other applications focused on the in-depth characterization of ion implants.[26,44–46]

A novel application for GIXRF is the characterization of well-ordered nanostructures, typically used in semiconductor fabrication. Here, nanopatterned surfaces such as lattice structures are fabricated in two or three dimensions to build state-of-the-art transistor architectures.[47] When GIXRF is performed on such nanostructured surfaces, the interplay between the XSW and the nanostructures is also two-dimensional: in addition to a change of the penetration depth perpendicular to the reflecting surface with increasing angle of incidence with respect to the surface (θ), there is also a pronounced effect in the orthogonal direction. Changing the angle of incidence with respect to the orientation of the nanostructure (Φ), e.g. the lattice lines, changes the penetration behavior of the incident radiation with respect to the sidewalls of the nanostructures.

This results in relatively rich fluorescence intensity maps as a function of the two incident angles. This additional angular dependence in GIXRF was first observed on chromium gratings in 2014,[48] but could not be fully described by a physical model until a new approach for the calculation of the X-ray standing wave field using finite elements (FEM) was adopted.[49,50] With FEM solvers, the X-ray standing wave field distribution can also be calculated for such highly oriented nanostructured surfaces, where the established codes using the matrix method fail.

In Fig. 1, the FEM-based calculations of the normalized 2-dimensional integrated XSW inside the TiO_2 (left) and the HfO_2 (right) for a nanoscale grating structure as shown in the inset are shown. Identical geometrical parameters for the nanostructure as determined in ref. 51 were used. It can be seen how the regularly ordered nanostructure leads to a strong additional dependence on the azimuthal angle Φ, which would not be observed for stratified layers or randomly ordered nano-objects. For more details on this special case of GIXRF, the reader is referred to 49–51.

2.2 Exemplary GIXRF calculations

To illustrate the basic relationships between different sample types and their corresponding GIXRF fluorescence signals, several simple cases are treated in the following. For direct comparability with GEXRF, the same sample systems will be treated later in Section 3.2.

As a first case we consider a thin homogeneous Ni layer (thickness is 1 nm) on a silicon substrate. When the photon energy of the excitation radiation is 9.5 keV and thus above the Ni–K absorption edge, Ni–K shell fluorescence can be observed. Both the intensity of this Ni–K shell fluorescence signal and the sample reflectivity versus angle of incidence are shown in Fig. 2. The GIXRF response of this sample follows the classical thin film behavior (see ref. 7) with the maximum at the critical angle of total external reflection of the underlying Si substrate for this incident photon energy. The peak is due to the fact that the XSW generated above the sample surface penetrates the thin film at $\theta = \theta_{crit}$ with its first maximum, resulting in (ideally) a twofold enhancement of the fluorescence signal with respect to high incident angles for which no XSW is present.

For comparison, the critical angle for total external reflection of Ni is also shown. Due to the higher optical density of nickel compared to silicon, it has a higher critical angle at 9.5 keV. The fact that the thin Ni layer does not affect the critical angle of the sample system indicates that it does not have a significant influence on the XSW. With increasing thickness of the Ni layer this changes gradually.

When the Ni layer is 10 nm thick, the resulting XRR and GIXRF signals change significantly. Fig. 3 shows the resulting calculations also for an incident photon energy of 9.5 keV. Compared to the thin film data, the XRR shows strong oscillations. They are caused by interference between radiation reflected from the surface and photons reflected from the silicon surface. Their frequency is also a good indication of the thickness of the Ni layer.[52]
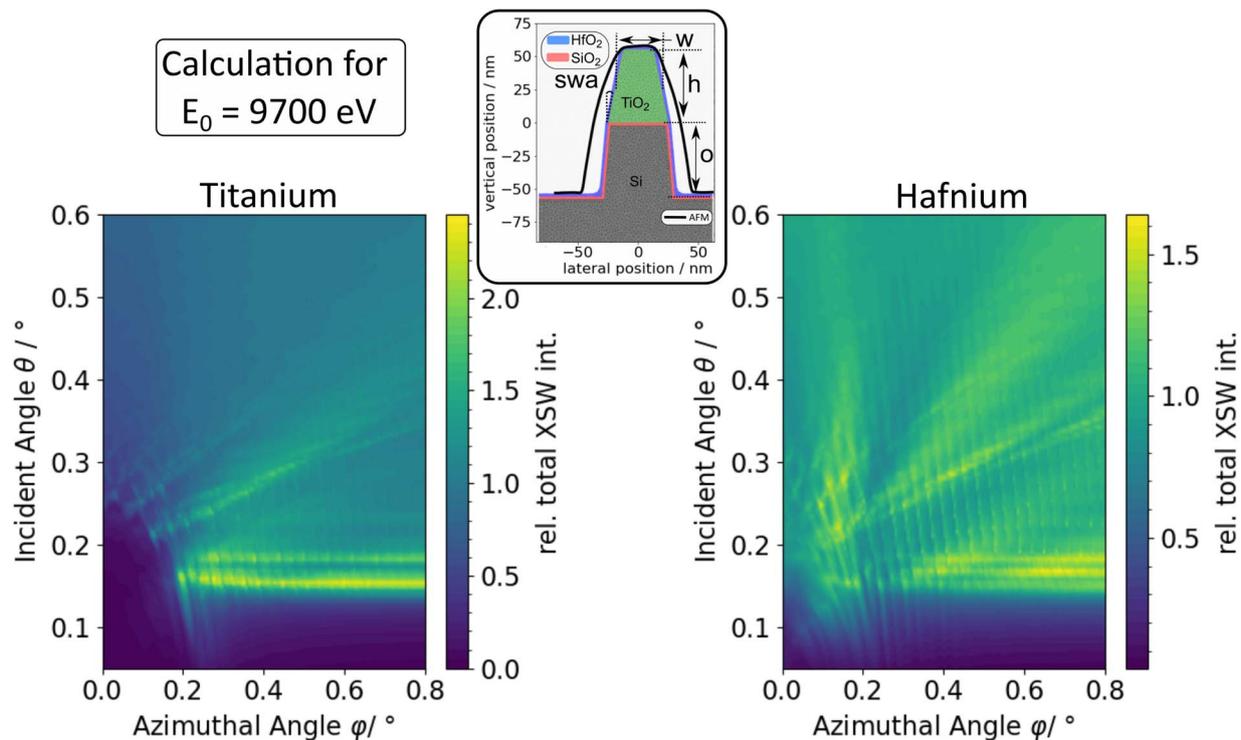
3370 | J. Anal. At. Spectrom., 2025, 40, 3368–3393

This journal is © The Royal Society of Chemistry 2025

Fig. 1 FEM-based calculation of the normalized 2-dimensional integrated XSW inside the TiO_2 (left) and the HfO_2 (right) for a nanoscale grating structure as shown in the inset. The geometrical parameters are taken from ref. 51.

In GIXRF, one would obviously observe a more intense fluorescence signal compared to the thin film example, but also the dependence on the incident angle changes quite drastically. The peak shifts to higher incident angles because the critical angle is now determined by the Ni layer, which can also be seen in the XRR data. In contrast to the thin film, it is not exactly at the critical angle. This is due to the fact that the integral intensity inside the layer, and thus the emitted fluorescence radiation, continues to increase above the critical angle. In addition, a weak second peak is visible that is coincident in position with the peak in the reflection curve, illustrating the

interdependency due to modulations in the XSW intensity. This can be nicely followed in the corresponding XSW field distribution shown in Fig. 4. The first peak of the fluorescence curve as well as the first and second peak of the XRR curve are marked with vertical dotted lines in both images. It can be clearly seen that at the critical angle for Ni (horizontal dashed line) a high local XSW intensity penetrates the surface of the Ni layer but not the entire layer. At slightly higher incident angles, the entire layer is probed, resulting in a higher overall fluorescence signal. The dotted line at $\theta = 0.627°$ indicates the first maximum of the
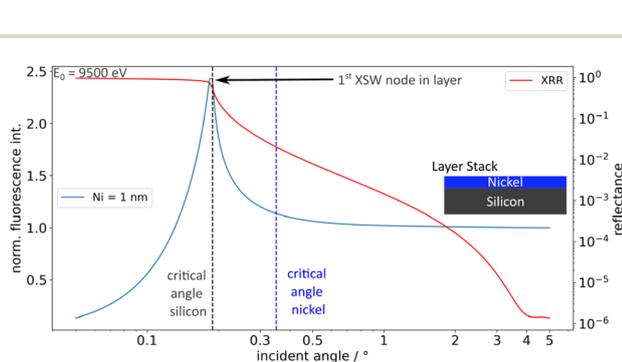

Fig. 2 Exemplary calculation of GIXRF and XRR response of a 1 nm Ni layer on a silicon substrate and an incident photon energy of 9.5 keV, which is well above the Ni-1s photoionization threshold of 8333 eV. The nominal critical angles for total external reflection of Si (0.189°) and Ni (0.351°) at this photon energy are also indicated by vertical dashed lines.
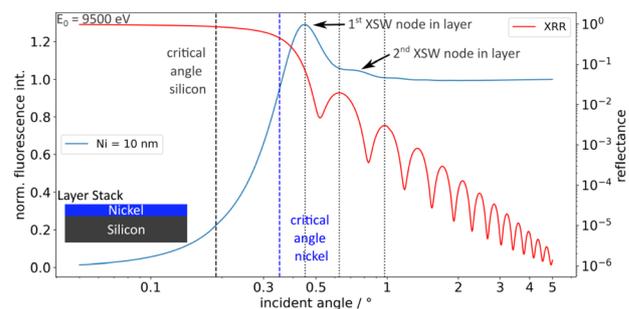

Fig. 3 Exemplary calculation of GIXRF and XRR response of a 10 nm Ni layer on a silicon substrate and an incident photon energy of 9.5 keV, which is well above the Ni-1s photoionization threshold of 8333 eV. The nominal critical angles for total external reflection of Si and Ni are also indicated by vertical dashed lines. The black dotted lines mark special positions in either the GIXRF or the XRR data and are explained in the text. They are also marked in the corresponding XSW depicted in Fig. 4.

This journal is © The Royal Society of Chemistry 2025

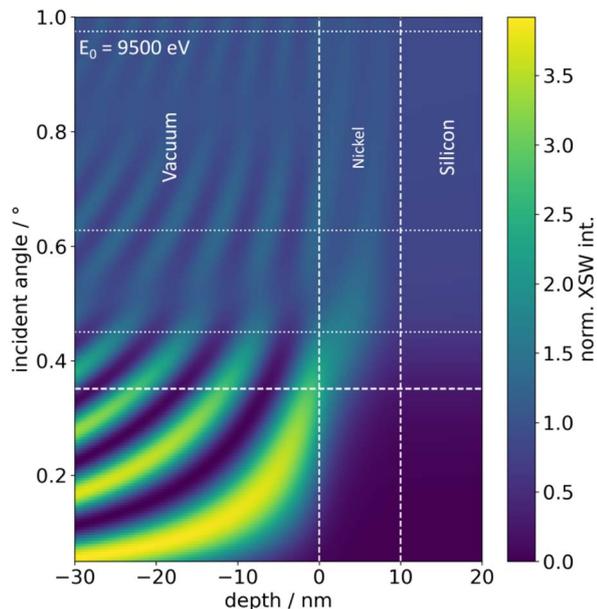*J. Anal. At. Spectrom.*, 2025, **40**, 3368–3393 | **3371**

Fig. 4 Corresponding XSW field for the calculations in Fig. 3. The vertical dashed lines indicate the position of the Ni layer. The horizontal dashed line indicates the critical angle for Ni and the three dotted lines the positions already marked in Fig. 3.
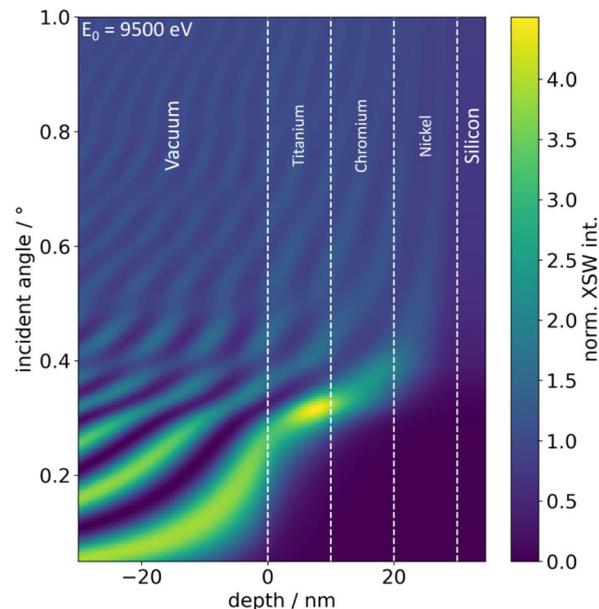
XRR curve. This increased reflectance results in larger XSW intensities as it is the interference between the incident (constant) and reflected (modulated as shown in the Fig. 3) waves. Similar behavior can be seen at the second XRR peak position at $\theta = 0.975°$.

As a more complex example, two more layers (Ti and Cr) are added on top of the Ni with a thickness of 10 nm each. For this example, the calculated GIXRF and XRR are shown in Fig. 5 and the corresponding XSW is shown in Fig. 6. The general behavior of the three GIXRF signals is very comparable as they all show a peak near the critical angle of the system and some oscillations slightly above. The angular positions of the first peaks of each layer increase as the layer moves deeper into the stack.
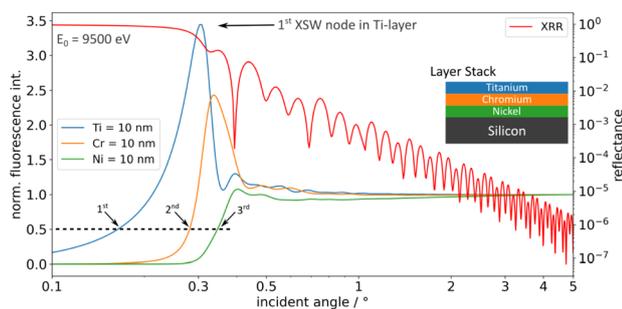

Fig. 5 Exemplary calculation of GIXRF and XRR response of a 10 nm Ti on 10 nm Cr on 10 nm Ni layerstack on a silicon substrate and an incident photon energy of 9.5 keV, which is well above the 1s photoionization thresholds of the three metals. The dashed line in the lower left corner at $y = 0.5$ helps to directly see the layer sequence from surface to the substrate as it correlates with the sequence of each layers fluorescence rising above the dashed level.

Fig. 6 Distribution of the X-ray standing wave field for the same layer stack as in Fig. 5 and an incident photon energy of 9.5 keV.

This demonstrates the simplest form of GIXRF depth profiling, as the sequence of layers can be inferred directly. However, the overall height of the fluorescence peak decreases as the layer gets deeper in the stack.

Both of these observations can be nicely explained by looking at the XSW field distribution in Fig. 6. The XSW penetrates deeper into the stack as the angle of incidence increases, resulting in the angular shift of each peak position. In addition, the total reflectance decreases and so does the total XSW intensity. This causes the fluorescence peak heights for the different layers to decrease.

In summary, these examples demonstrate the basic relationships between a sample's reflectivity *versus* angle of incidence, the X-ray standing wave field, and the observed GIXRF data. In a simple picture, a given material at a given position in depth interacts very differently with the XSW, resulting in a very different GIXRF signal. Using forward modeling schemes, the position of the material in depth, the distribution in depth and, if the instrumental setup allows, the amount of material can be determined.

2.3 Exemplary setups for GIXRF

In general, experimental setups for GIXRF based experiments do not differ much from typical instrumentation for *e.g.* total reflection X-ray analysis or X-ray reflectometry analysis. Obviously, one needs a monochromatic X-ray source with a collimated, parallelized exit beam or at least low angular divergence. Here, the required photon energy resolution should be below $10^{-3} \left(\frac{\Delta E}{E} \right)$. The sample must be able to be rotated with respect to the incident beam, the rotation axis needs to be contained within the sample surface plane and, of course, the generated X-
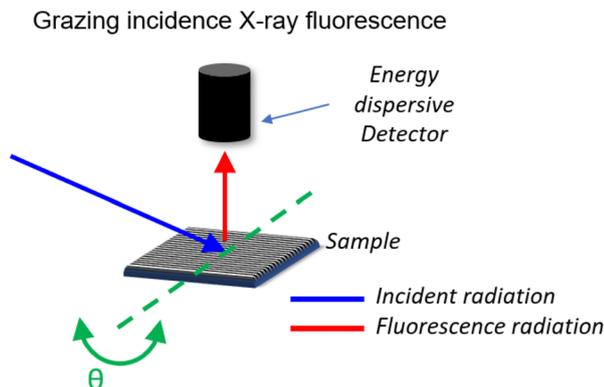
3372 | J. Anal. At. Spectrom., 2025, 40, 3368–3393

This journal is © The Royal Society of Chemistry 2025

Grazing incidence X-ray fluorescence

Fig. 7 Schematic view of a typical experimental arrangement for grazing incidence X-ray fluorescence analysis.

ray fluorescence radiation must be detected with an adequate detection system. Today, silicon drift detectors are usually chosen because they offer a very good count rate capability, which is important for GIXRF due to the high dynamic range of the substrate signals during an angular scan. A schematic view of the basic GIXRF geometry is shown in Fig. 7. The incident angle θ is usually defined as the angle between incident photon beam and sample surface and it is changed from zero up to a few degrees. The fluorescence detector is typically kept in fixed position in a nearly perpendicular position to the sample.

It is also quite useful if the vertical and horizontal intensity profile of the incident beam is known or can be determined, as it is a crucial input parameter for the calculation of the effective solid angle of detection Ω (see eqn (1)). The other necessary input parameter for this important value is the distance between the sample and the detector chip and, if necessary, the geometry of the collimator, the magnet or the entrance window of the detector. It is therefore necessary to ensure that these quantities can either be determined separately or that the effective solid angle can be derived for the particular setup using known samples as described for example in ref. 18.

In addition, the necessary degrees of freedom for accurate sample alignment must be available. The alignment must allow absolute knowledge of the incident angular scale. In addition, a common intersection of the center of the incident beam profile, the axis of rotation for the incident angle, and the center of the field of view of the detector and the surface of the sample must be ensured. This is critical for reliable interpretation of the recorded GIXRF data.

For a more detailed description of the needs and requirements of GIXRF setups, which are beyond the scope of this work, the reader is referred to the book by Klockenkaemper and von Bohlen.[7]

There are several sources of inspiration for GIXRF setups. Synchrotron-based GIXRF setups are used at the electron storage ring BESSY II in Berlin (Germany),[53] at the synchrotron radiation source Indus-2 (ref. 40) in Indore (India), at the SOLEIL synchrotron near Paris (France),[54] at the DELTA synchrotron in Dortmund (Germany)[55] and at the ELETTRA synchrotron in Trieste (Italy).[56]

The laboratory-based GIXRF setups typically use X-ray tubes as excitation sources and are usually custom-built instruments.[27,57–60] In recent years, however, commercial tools have also emerged and can be easily ordered for laboratory-based GIXRF applications.[14,36,61]

A commercially available instrument from Bruker has also been used to demonstrate, that upon proper characterization and calibration to determine the instruments geometrical and instrumental parameters,[14] depth-dependent and, more importantly, absolute quantitative information can be derived. The employed strategy for the instrument calibration is expected to be transferable also to other instruments, both custom-built or commercial.

3 Grazing emission X-ray fluorescence analyis

3.1 Theory of GEXRF

Based on the principle of microscopic reversibility, Becker, Golovchenko and Patel introduced grazing emission XRF.[8] The principle states that excitation and detection can be considered in reverse. Thus, GEXRF can be easily introduced based on the geometry of GIXRF by exchanging and inverting the paths for excitation and detection. As a further consequence, GEXRF intensity profiles can be calculated using the identical formula as for GIXRF, but with the photon energy of interest. This energy must be that of the photons propagating at a grazing angle with respect to the sample surface, which in GIXRF are the photons used for excitation but in GEXRF these are the fluorescence photons produced in the sample. Thus, for example, the formalism of Parratt[20] can be applied to calculate GEXRF intensity profiles, but models have also been developed that physically describe the refraction (reflection and transmission) of photons propagating at grazing emission models with respect to interfaces.[62–64] Detected interferences can then be explained by several possible detection paths and the difference in their path length. Depending on the grazing emission angle, the difference in path length can be a multiple of the wavelength of interest. This aspect explains why GEXRF is as suitable as GIXRF for depth profiling applications with nanometer sensitivity.

The depth range explored is dictated by the energy range of the fluorescence photons in GEXRF, whereas the energy of the incident photons is decisive in GIXRF. One can say that GIXRF limits the excitation of XRF to the near surface region, and GEXRF limits the detection of XRF to the photons emitted from the near surface region. When comparing GIXRF and GEXRF intensity profiles, it is helpful to normalize the angular scale to the critical angle. As in any application where modeling of X-ray refraction is required, accurate knowledge of the optical constants is therefore mandatory.

From an experimental point of view, however, there are some noticeable differences between GIXRF and GEXRF.[65–68] First of all, the requirement of longitudinal coherence (monochromaticity) of the incident radiation can be omitted. In fact, GEXRF has been realized with different excitation sources using

This journal is © The Royal Society of Chemistry 2025

J. Anal. At. Spectrom., 2025, **40**, 3368–3393 | **3373**

(focused) X-rays or charged particles. Examples using stand-alone X-ray sources,[8,67,69] synchrotron radiation,[70–72] laser plasma sources,[73,74] electrons[75,76] or protons[77,78] are reported. The requirements for GEXRF, such as collimated and monochromatic radiation, apply to the emitted radiation rather than the incident radiation. The fluorescence radiation is to be detected only under well-defined exit angles defined with respect to the sample surface. For this purpose, collimators and large sample-to-detector distances must be used so that a good angular resolution can be achieved, *i.e.* the angular broadening must be at least two orders of magnitude smaller than the critical angle for the energy of the fluorescence radiation used for the investigations. Angular intensity profiles are then recorded in a position sensitive manner by moving the detector in a circular or linear motion. Alternatively, wavelength-dispersive detection schemes,[65–68,72,73,79–83] which by design fix the detection direction due to the implemented optics (*e.g.* the Bragg condition on a diffraction crystal), or position sensitive detectors[51,69,74,84–87] also allow the selection of grazing emission angles with the required accuracy. In comparison, GIXRF setups are almost exclusively designed around energy dispersive detectors to achieve the best possible solid angle of detection.

However, it should be noted that care on the excitation selection should be taken when considering the modeling of recorded GEXRF intensity profiles where the goal is to retrieve the depth distribution of the atoms emitting fluorescence radiation. With X-ray sources and adequate excitation geometry, it can usually be assumed that the probability of excitation of fluorescence radiation is independent of depth, provided that the depth range of interest is much smaller than the penetration depth of the excitation radiation. This assumption cannot be made for particles due to their much shorter free path. In addition, the stochastic nature of the interaction of charged particles requires the use of Monte Carlo simulations to obtain the depth dependent excitation probability of the fluorescence radiation.

Regarding the longitudinal coherence requirement, it should be noted that the ratio of line width to energy of the characteristic radiation for K emission lines is about 5×10^{-4}. This ratio is very similar to the resolving power of the monochromators used for GIXRF. Thus, the requirement for a defined wavelength to realize grazing XRF experiments is met by nature. The experimental requirement is an energy resolving detection scheme that allows the discrimination of different photon energies so that the signal of interest can be separated from the background signals inherent in any experiment. Alternatively, and even if the different characteristic lines cannot be detected separately, these aspects have to be considered in the modeling of the GEXRF intensity profiles.

The consequences of these experimental differences affect the sensitivity of GEXRF, but also offer new possibilities. For a single grazing angle, the required collimation usually limits the solid angle of detection so that GEXRF is generally less suitable for the detection of trace impurities unless specific sample configurations are considered.[88] In the past, wavelength dispersive detection schemes, which can be easily combined with the grazing emission geometry, were also more suitable for the detection of

light elements although this situation changed with the advent of modern SDDs. The good compatibility between wavelength dispersive setups and the GEXRF geometry is given by the congruence between the required angular resolution and the typical angular acceptance of the diffractive gratings or crystals.

Finally, the measurement area is inherently large along the incidence direction in GIXRF, whereas in GEXRF it can be configured within certain limits by the cross section at the sample location of the radiation used to excite the fluorescence radiation and the angle of incidence used. This aspect is advantageous when localized measurements requiring a specific lateral resolution are required. It also allows to increase the sensitivity of the measurements by increasing the probability of excitation of the fluorescence radiation in the region close to the surface of the sample,[83,88] but care has to be taken about the possible effect on the angular resolution as large excitation spots on the sample degrade the exit angular resolution as the geometry towards the detector might change significantly in terms of distance and position within the spot. Similarly, soft X-rays, where L lines are measured instead of K lines, result in a larger fraction of fluorescence radiation generated in the near surface region, but the accuracy of the knowledge of the optical constants must be considered for an accurate interpretation of the measurements.

3.2 Exemplary GEXRF calculations

Similar to GIXRF in Section 2.2, some simple examples of the GEXRF response of layered samples are computed and shown below. For direct comparability between GIXRF and GEXRF, the same sample configurations are used and the GIXRF responses already discussed in Section 2.2 are also shown.

As a first example, the 1 nm thin Ni layer is considered an shown in Fig. 9. The same incident photon energy of 9.5 keV is used for the calculation, although it is not as critical for the GEXRF response as it is for GIXRF. In GEXRF, the primary question is whether the excitation energy can produce the fluorescence radiation one wants to measure. The critical angle of the sample stack, which determines the position of the maximum, depends on the photon energy of the observed fluorescence line, similar to the GIXRF case where the position depends on the incident photon energy. So in GEXRF the Ni-Kα_1 line is used for the calculation and the maximum is at the critical angle of silicon for photons with an energy of 7.478 keV (Ni-Kα_1 transition energy). Since this photon energy is lower than the 9.5 keV used for the GEXRF excitation, the critical angle of the system is larger and the GEXRF curve is shifted to higher angles. Otherwise, the observed signal is very comparable to the GIXRF case.

For the 10 nm thick Ni layer example, similar behaviour can be observed in Fig. 10. The Ni-Kα_1 GEXRF curve is shifted to higher incident angles as compared to the GIXRF curve and has a very similar shape. However, the enhancement in the vicinity of the critical angles is more pronounced in the GEXRF case. This is related to the fact that the optical properties of the sample are fairly different: in GEXRF, the photon energy of interest is below the Ni-K absorption edge, while in GIXRF it is

above. This results in a more than three times larger extinction coefficient for Ni in GIXRF and thus a significantly different attenuation behaviour.

With this behaviour in mind, also the seemingly different behaviour of the three-layer stack can be understood. As shown in Fig. 11, one might think at first that the GEXRF response is from a different sample than the GIXRF signal, since there is almost no difference in angular position between the signals of the different layers. In fact, the sequence observed in GIXRF is almost reversed in GEXRF, with the Ni showing first and Ti showing last a maximum in the angular intensity profile.However, this does not indicate a reversed layer sequence or even a mixed layer as one might think. Due to the drastically different critical angles for the respective relevant photon energies (see Table 1), the curves are stretched to higher incident angles as compared to GIXRF. Since the photon energy difference between GIXRF and GEXRF is largest for the Ti-Kα, this curve is stretched the most, the Cr curve slightly less and the Ni curve the least. This effect masks the layer sequence to some extent in GEXRF.

A simple way to unmask this effect is to plot the data against the wavevector Q instead of the emission angles. With $Q = 4\pi\sin\theta\frac{1}{\lambda}$, where θ is the emission angle and λ is the wavelength of the respective fluorescence line (in GEXRF) or the wavelength of the incident radiation (in GIXRF). By doing this, datasets obtained at different photon energies of interest can be easily compared as can be seen in Fig. 12. This also allows easy interpretation of the layer sequence in GEXRF or more direct comparison of GIXRF data with GEXRF data.

Finally, GEXRF is just as suitable for depth-profiling applications as GIXRF. Although the experimental geometry is reversed, one can think of it in a very similar way. From an experimental point of view one should keep in mind that the XSW is created by the interference of the fluorescence photons with themselves and not by the interference between incident and reflected photons as in GIXRF. Thus, each fluorescence line observed creates its own XSW resulting in the modified angular scales. As for GIXRF, forward modeling schemes can be used to determine the position of the material in depth, the distribution in depth and, if the instrumentation allows, the amount of material can be determined.

3.3 Exemplary setups for GEXRF

In typical scanning-based GEXRF setups,[66,68,81,90] components of the GIXRF setup can be retrieved, which is not surprising given

Table 1 Overview for the different fluorescence line energies relevant for the calculations in Fig. 11 and the resulting critical angles for total external reflection of Si and Ni taken from ref. 89

Case	Photon energy/keV	Silicon θ_{crit}/°	Nickel θ_{crit}/°
Ti-Kα	4.51	0.400	0.746
Cr-Kα	5.41	0.333	0.619
Ni-Kα	7.48	0.240	0.440
GIXRF	9.5	0.189	0.351

the reciprocal equivalence. In most cases, X-rays are being used, but charged particles were used as well. The latter offer the advantage of more efficient excitation of the near-surface volume of a sample, but in terms of modeling experimental data, the interaction volume is more difficult to calculate. This aspect makes depth profiling applications less straightforward than with X-rays, where a quasi-homogeneous excitation of the investigated atoms can be assumed for sufficiently thin depth distributions and sufficiently high incident X-ray photon energies and angles of incidence. In contrast to GIXRF, the X-ray sources used do not need to be collimated or monochromatized. While monochromatization can help to optimize the background conditions, a more relevant aspect is the sample area that is illuminated. In fact, the excitation should not be placed close (e.g. <1 mm) to the lateral sample boundaries to prevent fluorescence photons from escaping through the side of the sample. Furthermore, excessively large illumination areas can affect the angular resolution that can be achieved, which is the case when the volume from which the XRF photon can originate can no longer be perceived as a point source from the point of view of the detector. This requirement is more critical in the direction perpendicular to the axis along which the fluorescence radiation is detected.

The sample surface and sample positioning requirements are identical for both grazing XRF geometries. Compared to GIXRF, in GEXRF the XRF intensity changes due to a variation of the emission angle are monitored. Thus, the emission angle must be as well defined and controlled as the incidence angle in GIXRF experiments. The control and variation of the emission angle in the conventional scanning-based setups is usually realized by rotating the sample, but it can also be realized by moving the detection system. However, this solution requires a lightweight detection system to perform the motion with the required precision, accuracy, and reproducibility. This approach has the advantage of a constant angle of incidence for the radiation used to excite the fluorescence radiation.[91] In both approaches, the axis of rotation must coincide with the irradiated spot on the sample surface. If the detector is not position sensitive, the emission angle can be defined by an adjustable (double) slit collimator system placed in front of the detection system. Either way, the goal is to collimate the detected fluorescence radiation so that an accurate definition of the emission angle can be made. This requirement also introduces the main disadvantage of GEXRF, which is the small solid angle of detection per emission angle. The angular resolution of the system is determined by the aperture of the slits, their separation distance, and the separation distance to the irradiated sample system. Reported angular resolutions are in the order of mrad or less.[67,84,91] As is often the case in experimental physics, a trade-off between angular resolution and detection sensitivity must be made depending on the main experimental objectives (trace element control or structural surface characterization). A good angular resolution is required to separate possible interference fringes in the angular X-ray fluorescence intensity profile, e.g. for layered samples.[63,71,80]

For the detection system of the fluorescence photons, either energy dispersive detectors or wavelength dispersive setups can

This journal is © The Royal Society of Chemistry 2025

J. Anal. At. Spectrom., 2025, **40**, 3368–3393 | **3375**

be used. The main advantage of using energy dispersive detectors is the possibility to monitor several X-ray fluorescence lines of one or more elements simultaneously, which allows to obtain different data sets for one sample without changing the experimental setup.[67] The main advantages of wavelength dispersive setups are their energy resolution and good background rejection capabilities, which significantly increase the sensitivity to low-Z elements by better separating their fluorescence lines from other X-ray lines and by improving the signal-to-background ratio. This compensates for typically higher complexity and the lower detection efficiency due to the smaller (effective) solid angle of detection compared to energy dispersive detectors. For energy dispersive setups, the solid angle of detection is determined by the distance to and the aperture of the slit/detector system; for wavelength dispersive setups, it is determined by the area of the optics where the Bragg condition is met, the reflectivity of the optics, and the efficiency of the detector. Note that in most cases the angular selectivity of the optics is fine enough to avoid the use of slits to define the emission angle, provided that a position sensitive detector is used. This aspect allows to benefit from the advantages of wavelength-dispersive setups without being too much penalized by the small solid angle that characterizes wavelength-dispersive instruments. The low-Z sensitivity was one of the main motivations for the development of wavelength-dispersive GEXRF spectrometers[66] as a complement to GIXRF setups. Greater sensitivity to chemical states (when measuring X-ray emission lines where a valence shell is involved in the atomic decay process) and good separation of the many L-lines of mid-Z elements and/or M-lines of heavy elements are other advantages offered. The main drawbacks of wavelength dispersive setups are the aforementioned reduced solid angle of detection and, depending on the application, the reduced energy range that can be monitored. For this reason, wavelength-dispersive setups are not suitable for elemental determination of an unknown sample, as required in contamination control, for example, and GEXRF in conjunction with wavelength-dispersive setups is limited to applications where the angular intensity profile of an X-ray emission line of a target element is to be monitored.

The advent of pixelated, direct-detecting, position-sensitive detectors allowed the acquisition of complete GEXRF intensity profiles with unprecedented efficiency.[51,69,74,84–87] These detectors allow the simultaneous detection and discrimination of X-ray photons propagating from the sample at different emission angles. Thanks to the active area of such detectors, the different emission angles can be distributed on the detector in such a way that the angular range monitored is limited by the detector size and the sample-to-detector distance, while the angular resolution achieved is defined by the pixel size and the sample-to-detector distance. The GEXRF intensity profiles are then acquired in a single measurement at a fixed position of the setup components and no slit system is required. The first demonstration of this detection arrangement was realized with imaging plates, which provide a large detection area and good spatial resolution, thus a large covered range in grazing emission angles and good angular resolution.[92] The concept was reintroduced about 20 years later with digitized detection

schemes with improved signal-to-noise ratio.[84] No moving components are required and the XRF intensity is recorded simultaneously for all grazing emission angles. This static nature of the setups greatly simplifies the experimental requirements, since scanning-based setups, such as GIXRF or conventional GEXRF, require high accuracy in the angular rotation and the position of the rotation axis, which should coincide with the sample surface.

A scanning-free setup therefore reduces the experimental complexity to knowing the exact detection geometry, i.e. the distance and orientation with respect to the source of the XRF rotation and the pixel size. The only motion control required is to align the sample with respect to the coordinates of the array of the position sensitive detector used. The normal vector to the sample surface is in the best case parallel to the main axis (or one of the main axes) of the detector, and the detector is sufficiently large in this dimension to cover the full angular range from 0° up to 2–3 times the critical angle for the energy of interest. Considering the number of grazing angles for which XRF intensity must typically be recorded, these scaning-free setups allowed GEXRF intensity profiles to be obtained in similar acquisition times to GIXRF intensity profiles. Other advantages of the scanning-free setups are the insensitivity to source intensity variations, since the intensity at all emission angles is monitored simultaneously, and the absence of dead times and instabilities caused by motor motion.

As detectors, hybrid pixel detectors that allow single-photon counting have been used mainly at synchrotron radiation facilities where selective excitation of fluorescence radiation is possible.[84,93] CCD cameras in combination with adapted single-photon evaluation algorithms,[94–96] which allow to obtain both position- and energy-sensitive information and thus to discriminate different photon energies, allowed to extend the scope of GEXRF to simultaneous multielemental analysis.[51,69,97] The same is true for the use of pnCCD detectors.[51,74,87] Current detector developments[98–101] will allow to further extend the capabilities of scan-free GEXRF into the soft X-ray regime. Compared to the film plates used in the original development, all of these detectors offer digitized data, good sensitivity, signal-to-noise ratio, dynamic range, and linear intensity response.

A prerequisite for any scanning-free GEXRF setup (see Fig. 8) is that the difference in the angular range spanned by each pixel (emission and azimuthal if required) between adjacent pixels is fine enough. The angular step, or equivalently the aperture angle per pixel, must meet the requirements of the desired angular resolution, which is typically of the order of 1 permille to 1 percent of the critical angle of total external reflection. The main factor affecting the angular resolution for a given pixel size is the sample-to-detector distance. Together with the sample volume from which the fluorescence photons originate, this factor defines the aperture angles maintained by each individual pixel. This contribution can be evaluated geometrically. Angular resolution and solid angle must then be balanced against each other. For the sample volume contribution, the lateral dimension on the surface is usually more important, since the probed depth range, which varies with the grazing
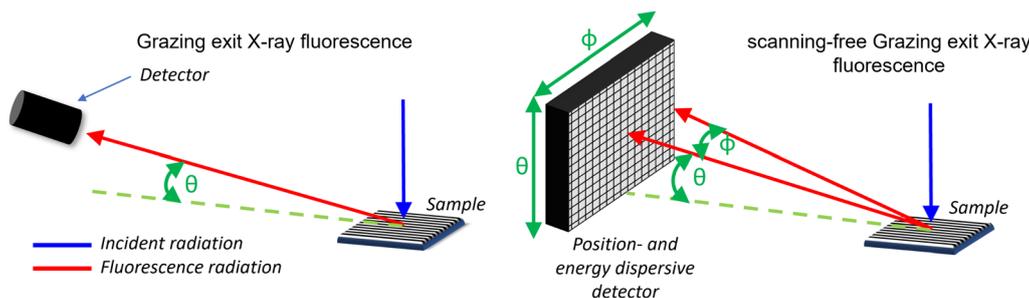
Fig. 8 Schematic view of a typical experimental arrangement for grazing emission X-ray fluorescence analysis and for scanning-free GEXRF, where pixelated detectors are used to record many different emission angles at once.

emission angle,[102] is usually much smaller than the pixel size. When pixels with different azimuthal angles but similar emission angles are summed to obtain the GEXRF intensity profile, another broadening factor can be introduced by the allowed variation in emission angle between the different pixels.

For samples with lateral homogeneity on the surface, pixels with the same emission angle can be summed to obtain the GEXRF intensity profile. In these cases, the size of the detector in the non-dispersive direction results in an increased solid angle of detection compared to standard scan-based setups, which together with the simultaneous monitoring of different emission angles contributes to the overall efficiency of the setup and drastically reduces acquisition times. The sensitivity to both the grazing emission angle and the azimuthal emission angle (different pixels that span the same emission angle but have a horizontal position resulting in a different azimuthal angle) of the sample under investigation allows to extend the range of applications to well-ordered nanostructures.[51,86,93] Compared to conventional GIXRF and GEXRF setups for such investigations,[49,103] the dimensions to be scanned are reduced.

3.4 Combination GIXRF and GEXRF setups

Combinations of grazing incidence and emission geometries have also been realized in the past to simultaneously benefit
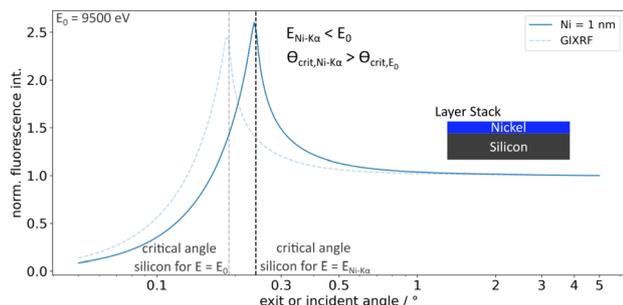

Fig. 9 Exemplary calculation of the GEXRF response using the Ni-Kα_1 fluorescence line (7478 eV) of a 1 nm Ni layer on a silicon substrate and an incident photon energy of 9.5 keV. The corresponding GIXRF response is indicated as a dashed curve. The nominal critical angles for total external reflection of Si for both the incident photon energy and the fluorescence line energy are also indicated by vertical dashed lines. As $E_{Ni-K\alpha} < E_0$ both the critical angle and the observed signal shifts to a higher theta.

from the surface sensitivity of both techniques. The simultaneous collimation of the incident and emitted X-rays resulted in a reduced experimental efficiency. The main motivation for the realization of these geometries was the very low background, since both the excitation and the detection process are focused on the near-surface region. To better control the depth range explored in the sample, both grazing angles are varied, resulting in extensive data sets.[104,105] The measured interference patterns depend on the incident and emitted photon energies and vary with the angle of incidence and emission. The analysis of thin films, layers, interfaces and impurities have been the main topics of application.[106–108]

4 Classes of typical applications of GIXRF and GEXRF

The angle dependent information obtained from grazing XRF experiments is used for two main purposes, depth profiling applications and self-consistent validation or falsification of TXRF based quantification results.

Depth profiling applications have been carried out on various classes of samples where vertical dimensions in the nanometer range are of interest. In order to obtain structural information in addition to elemental information, it is necessary to measure the X-ray fluorescence intensity dependence on the grazing emission angle. These studies typically include (multi-)layered samples, nanoparticles and implantation profiles. The basic principle is to vary the interference pattern leading to a pronounced variation in the detectable fluorescence radiation in the angular range below the critical angle(s) of total reflection defined by the interface(s) within the sample and to tune the depth range from which the fluorescence radiation can originate in the angular range above the critical angle(s) of total reflection.

4.1 Layers

Thin films or coatings with layer thicknesses in the range of a few nanometers to hundreds of nanometers can be produced, for example, by atomic layer deposition (ALD),[109] physical vapour deposition (PVD) or chemical vapor deposition (CVD).[110] In technological or scientific applications, the thin films are used to modify the thermal, mechanical, optical, chemical or
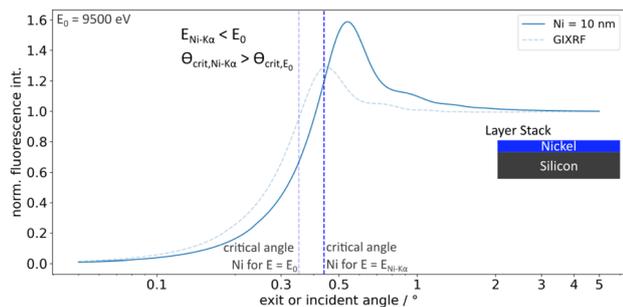
This journal is © The Royal Society of Chemistry 2025

J. Anal. At. Spectrom., 2025, **40**, 3368–3393 | **3377**

Fig. 10 Exemplary calculation of the GEXRF response using the Ni-Kα₁ fluorescence line (7478 eV) of a 10 nm Ni layer on a silicon substrate and an incident photon energy of 9.5 keV. The corresponding GIXRF response is indicated as a dashed curve. The nominal critical angles for total external reflection of Ni for both the incident photon energy and the fluorescence line energy are also indicated by vertical dashed lines. As $E_{Ni-K\alpha_1} < E_0$ both the critical angle and the observed signal shifts to a higher theta.
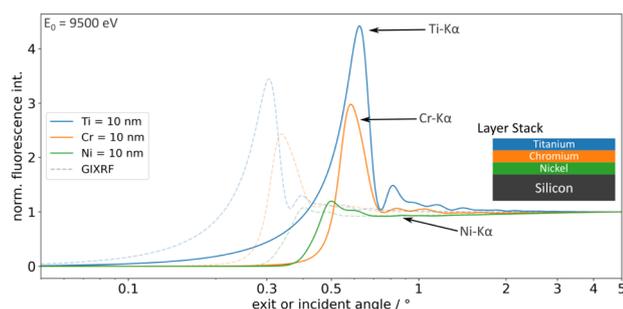

Fig. 11 Exemplary calculation of GEXRF responses for the Kα₁ fluorescence lines of a 10 nm Ti ($E_{K\alpha_1}$ = 4511 eV) on 10 nm Cr ($E_{K\alpha_1}$ = 5415 eV) on 10 nm Ni ($E_{K\alpha_1}$ = 7478 eV) layerstack on a silicon substrate and an incident photon energy of 9.5 keV. The dashed lines indicate the corresponding GIXRF responses as discussed in Fig. 5. As the corresponding fluorescence line energies determine the critical angles and the angular dependence of the underlying XSW, the sequence of each layer's signal is not directly showing the layer sequence.

Fig. 12 Exemplary calculation of GEXRF responses for the Kα fluorescence lines of a 10 nm Ti on 10 nm Cr on 10 nm Ni layerstack on a silicon substrate and an incident photon energy of 9.5 keV. The dashed lines indicate the corresponding GIXRF responses as discussed in Fig. 5. In contrast to Fig. 11, the data is plotted against the probed wavevector Q.

electrical properties of a system. Examples include surface modification applications, chemical sensors, photo or electrochemical systems, semiconductor devices or optics in the optical or X-ray range (lenses, mirrors and multilayers).Grazing XRF, *i.e.*, GIXRF and GEXRF, can contribute to the characterization of the layers produced by assessing the thickness, as shown in Fig. 13 but also in part the mass density of the thin films produced. The latter is the most important aspect to consider, since the expected reduction in mass density for structures with nanometre dimensions will affect the optical properties of the material. The same applies to surface oxidation or low-Z contamination, which can occur when materials are exposed to intense X-ray radiation. Another noteworthy aspect is that the determination of layer thickness and mass density provides access to the mass deposition, which can be separately determined by *e.g.* quantitative XRF analysis through dedicated experiments. The advantage of separately quantifying mass deposition is that this complementary information
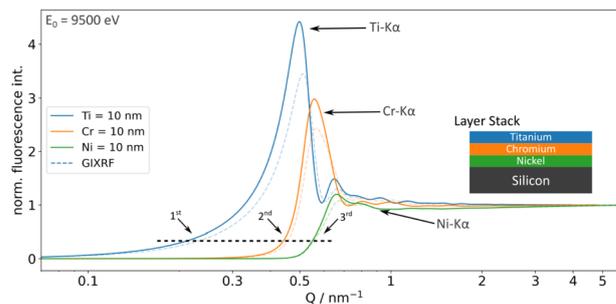
provides a means of validating the modeling of grazing angle XRF intensity profiles, where the layer thickness and mass density can be used as fitting parameters. In this way, structural and analytical information can be combined for a more robust and reliable interpretation of the experimental data, since the mass density is directly related to the optical constants used for modelling refraction effects.[12]

The quantification of the mass deposition is best realized in the angular regime above the critical angle for total external reflection, where no X-ray standing wave field (XSW) has to be considered, so that a more accurate determination of the mass deposition is possible. Quantification requires the assessment of instrument-related parameters, *i.e.* the intensity (and possibly spectral distribution) of the incident X-rays, the (incidence angle dependent) solid angle of detection and the photon energy dependent detection efficiency (after deconvolution of the fit of the experimental XRF spectra). These can be assessed either by (radiometric) calibration of the different parts of the instrumentation or by performing reference measurements to at least assess the combined information on these parameters. In the former case, the reference-free XRF scheme allows a forward-calculation of the experiment performed,[15] in the latter case, care must be taken to ensure the transferability of the calibration strategy to the actual sample type.

Thin films and multilayers have been investigated in terms of layer thickness, mass density, and in some cases mass deposition, using the depth profiling capabilities of GIXRF, *e.g.*, in ref. 13, 21, 24, 28, 29, 31, 33, 36, 38–40, 61 and 111–125 or GEXRF, *e.g.*, in ref. 65, 67, 74 and 126–129. Note that the oscillations observed in the Cr fluorescence radiation emitted by a three-layer sample consisting of Cr/Au/Cr layers deposited on quartz glass were interpreted as experimental evidence for the reciprocity theorem between GIXRF and GEXRF.[130]

GIXRF based studies often assume a layered model with homogeneous and discrete layers to fit the data by inverse modelling. This formalism was first introduced by L.G. Parratt[20] and has been adapted, for example, into a matrix formalism to simulate the propagation of an electromagnetic wave through a stratified medium.[131,132] Care must be taken to ensure physically reasonable modelling for reliable interpretation,[111,114]

3378 | *J. Anal. At. Spectrom.*, 2025, **40**, 3368–3393

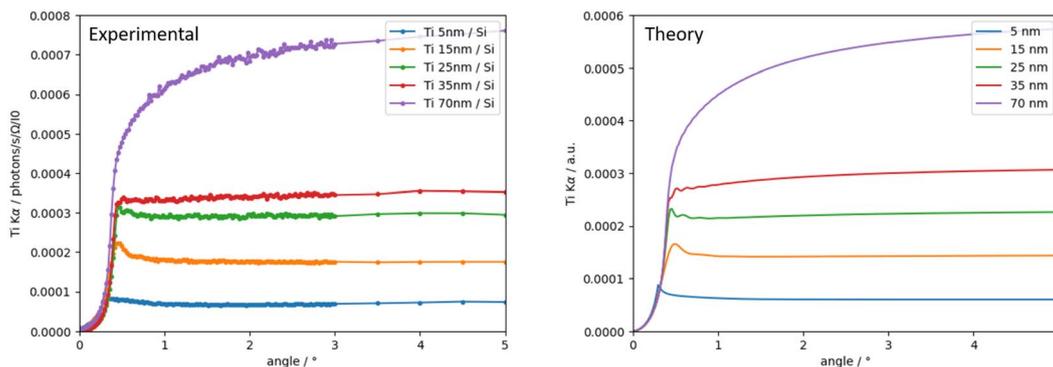This journal is © The Royal Society of Chemistry 2025

Fig. 13 GIXRF measurement on Ti layers at an incident photon energy of 6 keV (left panel) and corresponding theoretical dependence (right panel), illustrating the sensitivity of GIXRF to the varying layer thicknesses.

surface roughness[133–135] and the coherence length of the X-ray source.[136,137] Besides the mentioned mass density reduction and oxidation, all these parameters have to be taken into account in the calculation of the XSW, which in the case of modelling has to be iteratively adapted and recalculated in order to optimise the model towards reproducing the experimental data, assuming that the variation of the solid angle of detection with the grazing angle of incidence, the XRF detector has been operated in its linear regime over the full angular range[138] and the incident intensity variations with time have been correctly accounted for.

An experimental advantage of GIXRF investigations is the possibility of simultaneous acquisition of X-ray reflectivity (XRR) during the GIXRF measurement. This allows an analytical and a dimensional technique to be combined in a single experiment. A combined evaluation of the data, based on the optical constants of the different layers involved, enables obtaining mutually validated results with reduced errors for layers with thicknesses ranging from a few nanometers to a few hundred nanometers. This combined information has recently been exploited in several examples.[13,19,27,33,35,36,42,119,139–142]

In this context it can be mentioned that several software packages for the calculation of the XSW pattern[22] and the GIXRF intensity profiles and corresponding XRR curves have been presented in the literature.[17,25,143] In GEXRF based investigations, the developments from GIXRF can be used based on the reciprocity theorem[8] to derive the desired information by exchanging the energy of the incident photons against the energy of the fluorescence photons to account for which X-rays propagate at a grazing angle with respect to the interfaces where refraction takes place. An alternative approach is provided by the formalism developed by Urbach and de Bokx.[63,64] Here the angular intensity profile is calculated by summing the contributions of the X-ray fluorescence emitting sources after taking into account their distribution within the sample. The derived equations allow direct consideration of the factors that may influence the GEXRF intensity profile by inserting them as fitting parameters. This aspect has been exploited to investigate separately the influence of layer thickness, layer oxidation, bulk density reduction and surface roughness for the example of different Al layers on the top of Si wafers.[65] Compared to the

layered model strategy, the derived analytical equations allow to reduce the number of calculation steps and free fitting parameters.

A comparison between the results obtained for multi-layered samples using either GIXRF or GEXRF, but the same data evaluation formalism, is presented in 144. The results were largely in agreement and deviations were attributed to the optical constants, which only emphasizes the need for accurate determination of the latter.

4.2 Nanoparticles

Nanoparticles are of interest because tuning their elemental composition, size and shape allows them to be used in medical and pharmaceutical sciences, catalysis, photovoltaics, spintronics or nano- and biotechnology, among others. Indeed, the properties of nanoparticles differ significantly from those of bulk materials due to the large surface-to-volume ratio, offering a larger ratio of atoms or molecules with fewer neighbors and bonds than in a bulk matrix.[145] However, tailoring nanoparticles to desired sizes and shapes remains a challenge. Consequently, analytical techniques capable of characterizing nanoparticles in terms of these parameters are required to study their correlation with physical or chemical properties, *e.g.* their catalytic activity, in relation to specific applications. Often nanoparticles are prepared in solution, but some applications, such as nanofabrication,[146] nanoelectronics[147] or quantum dots,[148] require the deposition of nanoparticles on the surface of a flat substrate. This type of sample meets the requirements for grazing angle XRF.

It should be noted in this context that other analytical techniques, such as non-contact atomic force microscopy or electron- or ion-based techniques, also provide morphological information on nanoparticles, but not on the ensemble of nanoparticles. Only a fraction of the nanoparticles is examined until a fraction considered statistically relevant is examined. Grazing XRF techniques provide averaged information on all nanoparticles. The measurements are not affected by the electrical or magnetic properties of the substrate and can even be considered to be realized under ambient conditions. With this in mind, GIXRF and GEXRF have been used to determine nanoparticle morphology[139,149–156]

This journal is © The Royal Society of Chemistry 2025

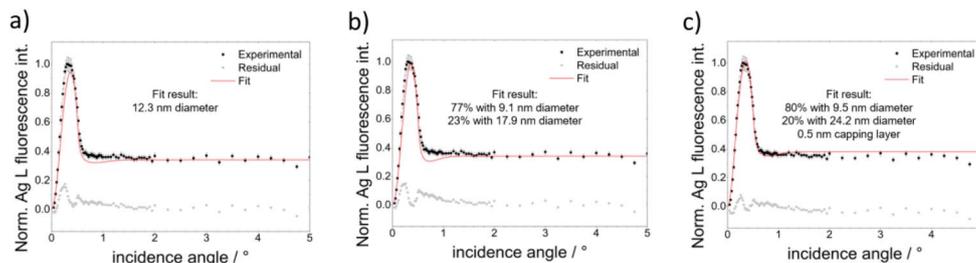*J. Anal. At. Spectrom.*, 2025, **40**, 3368–3393 | **3379**

Fig. 14 GIXRF measurement on Ag nanoparticles with two different sizes at an incident photon energy of 3.5 keV, where it is shown that the polydispersity as well as the presence of a passivating capping layer need to be taken into account to properly reproduce the experimental data. If only one particle size is assumed (part a) or if the capping is neglected (part b), the experimental data cannot be fully reproduced. The interpretation was supported by scanning electron microscopy and atomic force microscopy.

When investigating nanoparticles deposited on the surface of a substrate, grazing XRF offers further advantages. The penetrating properties of the X-rays make a large dynamic range of nanoparticles accessible, from a few nanometers to several hundred nanometers. In addition, the grazing geometries result in a significant reduction in background contributions from the bulk volume. Add to this the fact that the angular range of interest is mostly below the critical angle of total external reflection attributable to the bulk matrix for the wavelength of interest, and it becomes clear that almost background-free experimental investigations are possible. Either the incident X-rays cannot propagate into the bulk volume (GIXRF) or the X-rays emitted from the bulk volume cannot reach the detector due to refraction at the substrate-vacuum (or air) interface (GEXRF). In both cases, only an evanescent wave propagating along this interface can contribute to the measurement signal and the proven depth range from the substrate is only about 3 nm to 5 nm. The contributions from the bulk volume and the nanoparticles can also be distinguished by their different photon energies. For grazing angles above the critical angle, the contribution of the bulk signal increases to a first approximation linearly with the grazing angle.

Below the critical angle of total external reflection, the sensitivity to fluorescence radiation from the nanoparticles is further enhanced by the interference effects between X-rays propagating at a grazing angle with and without reflection at the substrate-vacuum (or air) interface. Depending on the difference in path length, constructive interference is possible, resulting in a fourfold increase in intensity under ideal conditions. The modulation of this interference pattern with the incident angle also provides information about the size and shape of the nanoparticles deposited on top of the substrate. To do this, it is necessary to know the refractive index of the substrate for the energy of the X-ray photon of interest. Using this knowledge, the dependence of the X-ray intensity as a function of the grazing angle in the angular range from 0° to the critical angle allows to obtain information about the size and shape of an ensemble of nanoparticles.

Extracting this type of information is easiest when the assumption of a mono disperse, low density surface coverage of nanoparticles can be validly made. For small nanoparticles, *i.e.* sizes in the range of only a few nanometers, the assumption that all atoms emitting fluorescence radiation are located in the same plane directly on the top of the substrate is valid,[63,157] since in this size regime no sensitivity to different shapes can be achieved.[154] For larger nanoparticles, the change in nanoparticle cross-sectional area with increasing distance to the substrate-vacuum (or air) interface must be considered in the calculation and modeling of angular intensity profiles.[139,154] Sensitivity to different nanoparticle shapes and even discrimination of core and shell volumes of multi-element nanoparticles with a more complex structure can be realized. Nanoparticle dimensions between about 10 nm to over 100 nm[157] can be studied most reliably. The lower limit is given, as mentioned, by the small differences in the angular intensity profiles, the upper limit is given by the angular resolution of the detection system.[154]

When considering poly disperse nanoparticle distributions, it has been proposed to calculate the grazing XRF intensity profiles of different nanoparticle sizes (bins), as shown in Fig. 14 and consider a weighted sum of the intensity profiles resulting from the different size contributions to fit the experimental data.[153] In this way, a coarse size distribution of the nanoparticles may become accessible.

In the case of higher surface coverage of nanoparticles, it becomes necessary to take into account the attenuation of the X-rays[158,159] and to include the presence of the nanoparticles in the calculation of the grazing XRF intensity profiles.[156] Indeed, in the low surface coverage approximation, it is assumed that the optical constant of the medium above the substrate is 1 (vacuum or air environment) and that any material present just above the interface is sufficiently diluted to have no appreciable effect on the optical properties. As the surface coverage increases, the optical properties at the top of the substrate change and the refractive properties at the interface change. To calculate the grazing XRF profiles, an effective density approach can be selected in the volume above the refracting interface.[156]

The angular range above the critical angle of the substrate for the X-ray photon energy of interest can be used for quantification. No refraction effects at the interface need to be considered as the reflectivity has decreased to 0 and the transmittance has increased to 1. The XRF intensity is no longer disturbed by deviations from the linear intensity response due to interference.[159,160] Together with the information on the size and shape of the nanoparticles, the quantification allows to estimate the surface coverage, although due to possible

3380 | *J. Anal. At. Spectrom.*, 2025, **40**, 3368–3393

This journal is © The Royal Society of Chemistry 2025

background contributions from the substrate, secondary fluorescence and different matrix effects may have to be considered in this angular range.[160–163]

Finally, it is worth mentioning that all the above considerations have been made on the basis of lateral homogeneity of the surface coverage, but that this aspect may need to be experimentally included and considered in the modeling of experimental data.[156]

4.3 Ordered nanostructures

The study of nanoparticles deposited on top of a microscopically smooth and macroscopically flat substrate was simplified by the random lateral distribution of the nanoparticles, which reduced the degrees of freedom. The random nature of the surface distribution made GIXRF and GEXRF measurements insensitive to rotation of the surface plane about its normal vector. The same angular fluorescence intensity profile is expected regardless of the azimuthal angle, defined as the angle between an arbitrarily defined vector contained within the sample surface plane and the vector for 0° incident X-rays (GIXRF) or X-rays emitted at 0° (GEXRF).

This situation changes when nano-sized surface patterns are considered, which are repeating objects of the same size that have periodicity in one or both of the orthogonal axes that

Fig. 15 This image shows the data from the work of Reinhardt,[48] where Cr stripes were analyzed employing GIXRF. The top part depicts the definition of ϑ and φ whereas the two other panels show the observed GIXRF data as a function of these two angles as well as an initial interpretation. For further details the reader is referred to the original paper.

define the surface plane of the substrate. These regularly structured nanopatterns, e.g. line or array structures, exhibit sensitivity to the probing or detection direction: the angular intensity profiles in GIXRF and GEXRF change with the azimuthal angle, defined here with respect to one of the symmetry axes of the nanopatterned surface structure.[48,103,164] This is shown in Fig. 15, where the data from ref. 48 are shown. The top part depicts both the employed Cr stripes and the definition of θ and ϕ. The two other images show the observed GIXRF data as a function of these two angles as well as an initial interpretation shown as red dotted curves.

Applications of such nanostructured patterns are mainly found in the semiconductor industry, where increasing down scaling is combined with more complex architectures.[165] Other technical examples include surface-enhanced Raman scattering (SERS) and surface-enhanced infrared absorption spectroscopy (SEIRA),[166] advanced light trapping applications in solar cells[167] or field emitter arrays.[168] The common aspect is that the dimensional and compositional characteristics of the nanostructured patterns affect the performance and properties of the realized devices. Grazing XRF techniques allow access to both of these characteristics in nanopatterned arrays on a representative ensemble of the structures without being affected by the electromagnetic properties of the materials. As such, grazing XRF techniques provide a complementary approach to the more commonly used X-ray or electron microscopy techniques, which provide access to individual objects. Other techniques either have physical limitations with current sample sizes, do not provide access to buried structures or require time-consuming and destructive sample preparation. It has been shown that grazing XRF techniques, by simultaneously probing the variation of XRF intensity with grazing and azimuthal angle, allow the extraction of element-sensitive information on the lateral and depth distribution of the elements and thus on the size and periodicity of the nanoobjects contained within an array.[49–51,86,93,103,169–174] The data modeling required for the interpretation of these spectra required more complicated models and novel numerical tools.[49,50,169,174–176] These allowed to add to the well-known depth profiling capabilities of grazing XRF techniques the lateral sensitivity to one- or two-dimensional periodically ordered nanosized objects, and to realize the calculations required for modeling experimental data on realistic time scales.

4.4 Implantation profiles

Doping by ion implantation or diffusion enables tailoring the physical, chemical and electrical properties of materials, particularly for semiconductor devices. In actual devices, the depth range of the material to be doped is limited by the other design features. Due to the down-scaling of device sizes, shallower implantation profiles had to be realized in order to maintain device functionality.[12] When investigating the continuously varying depth profiles, with depth ranges of only a few tens of nanometers, the doping process is affected. For ion implanted substrates, similar to bulk samples, no interference effects can be observed in grazing XRF intensity profiles due to
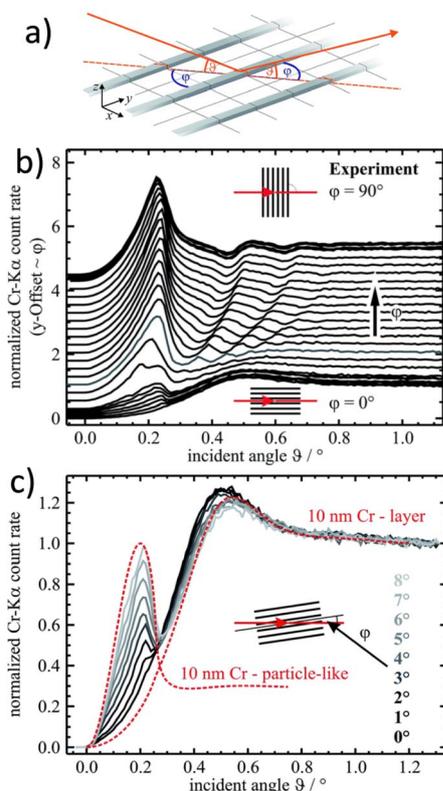
This journal is © The Royal Society of Chemistry 2025

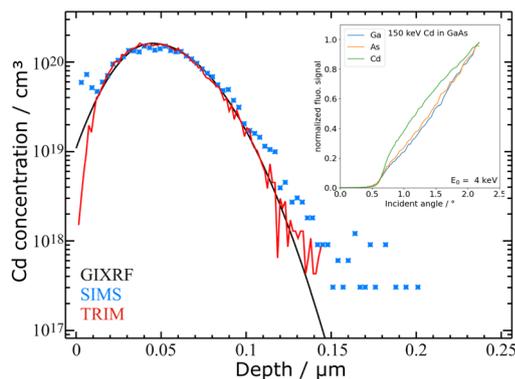*J. Anal. At. Spectrom.*, 2025, **40**, 3368–3393 | **3381**

Fig. 16 Exemplary GIXRF depth profiling result for a 150 keV Cd ion implantation into GaAs in comparison to secondary ion mass spectrometry and a TRIM calculation.[184] In the upper right corner, the obtained GIXRF angular fluorescence profiles are shown for Cd and the matrix elements. The excitation photon energy was 4 keV.

the presence of only one interface where X-rays can be refracted. The grazing dependence of the XRF intensity depends on the XSW intensity distribution above the sample surface, its penetration behavior at a given grazing angle and the number and in-depth distribution of implanted ions contained therein. Thus, a measured grazing XRF intensity profile allows in principle to reconstruct the spatial depth distribution of the implanted atoms, since the probed depth range is changed from a few nanometers to several tens or hundreds of nanometers.[7,12,14,17,26,44–46,83,177–183] The depth profile to be evaluated changes monotonically and, for implantation energies in the sub-100 keV range, is usually well within the depth range accessible at the largest grazing angle. For very light elements such as boron, the accessible depth range is of course lower due to the strong attenuation effects. An exemplary GIXRF depth profiling result for a 150 keV Cd ion implantation into GaAs in comparison to secondary ion mass spectrometry and a TRIM calculation[184] is shown in Fig. 16. In the upper right corner, the obtained GIXRF angular fluorescence profiles are shown for Cd and the matrix elements. The excitation photon energy was 4 keV.

An assumption often made in the reconstruction of the depth distribution of ion-implanted dopants from GIXRF or GEXRF data is that the optical constants of the substrate are not, or only negligibly, affected by the presence of the dopant atoms. Without this assumption, depth-dependent changes in the optical constants of the substrate must be taken into account, making the reconstruction of the depth profile a nonlinear problem. Especially for high-dose and low-energy ion implants, where a high local concentration of the implanted material inside the matrix can be realized this assumption may lead to wrong results.[26] The retrieval of the dopant depth distribution from the grazing XRF intensity profile is, regardless of this assumption, an ill-posed problem,[67] which means that there is no unique, unambiguous solution to the mathematical problem. Thus, physical feasibility needs to be included in the search for a solution to the inversion problem, where the elemental depth distribution is obtained from angular intensity

information of an X-ray fluorescence line from that element. Due to experimental noise and numerical errors either the use of regularization methods[79] or the maximum entropy method has been suggested[185] as an alternative to using an analytical description of the implantation profile for modeling the experimental data.[12,83,179,186]

4.5 Combination with XAS

GIXRF and GEXF can also be combined with X-ray absorption spectroscopy (XAS) for elemental chemical speciation, for example to study the oxidation or spin state of a metal by probing its electronic configuration. This is done by scanning the incident photon energy around the binding energy of a subshell of the element of interest. The most commonly used subshells are K or L3. However, this requirement to tune the incident photon energy around an ionization threshold may have serious implications for GIXRF measurements. Indeed, the optical constants of the matrix(es) (i.e. the elemental combination(s) within the layer(s) separated by interface(s)) depend on the incident photon energy and therefore vary strongly around the ionization threshold. As a result, the critical angle(s) and penetration depth or attenuation length may vary significantly during the XAS measurement, which is detrimental to meaningful interpretation of the data. While this may not be a problem if the element of interest is contained within a single (sub-)monolayer, or less of a problem if the angle of incidence is kept fixed above the critical angles encountered during the scanning of the incident photon energy, it needs to be mitigated in other situations. To this end, it has been proposed to vary the angle of incidence when tuning the incident photon energy in order to keep the penetration depth of the incident X-rays at a roughly constant value,[187] but this approach requires accurate knowledge of the optical constants of the sample for different incident photon energies. This knowledge cannot be based on tabulated values alone, but should also include the fine structure around the absorption edge. By repeating such measurements for different penetration depths, it was even possible to perform depth resolved chemical speciation measurements using the combination of GIXRF and XAS.[188] If only the near-surface region is of interest, a grazing angle of incidence below the smallest critical angle can be chosen such that total reflection conditions are satisfied for all incident photon energies.[189]

The situation is different when realising XAS measurements using the GEXRF geometry. Here the energy of interest, which defines the optical constants and the penetration depth, is that of the monitored XRF line (for which the tabulated values may be more reliably known, provided there is no ionization threshold for other elements present in the sample in the vicinity). Thus, these parameters do not vary throughout the XAS measurement and the depth of penetration is therefore constant.[190] In fact, for a typical sample and configuration for GEXRF measurements, the penetration depth depends only on the energy of the fluorescence photons and not on the energy and angle of incidence of the incident probe X-ray photons. This is true as long as the penetration depth of the incident X-ray

3382 | J. Anal. At. Spectrom., 2025, 40, 3368–3393

This journal is © The Royal Society of Chemistry 2025

photons is not too shallow compared to the depth range where the element of interest is contained. Therefore, in general, there is no need to make grazing angle corrections when varying the incident photon energy. A resulting advantage is that distortions due to a varying probe depth in the XAS measurements, often referred to as self-absorption,[191,192] do not need to be considered in the GEXRF geometry. Another advantage is that depth-resolved XAS measurements can then be easily realized by simply varying the grazing emission angle to a different position after each XAS measurement. In combination with a scanning-free GEXRF setup, simultaneous detection of the XRF line of interest is achieved for all grazing angles or, in other words, probed depths. By simply varying the incident photon energy around an ionization threshold, depth-resolved XAS measurements can be performed with good energy resolution[87,193–195] or, if only larger depth ranges are of interest, with coarser depth resolution using shorter sample-to-detector distances.[196–199] The combination of scanning-free GEXRF and XAS was further developed for time-resolved studies with a novel wavelength-dispersive setup, which allowed the surface oxidation of Cu and the formation of different species during this process to be followed.[200]

4.6 Self-consistent quantification

The surface sensitive nature of grazing XRF has been used for quantification purposes, for example to detect trace amounts of impurities on or inside wafers.[88,201] These applications consider data collected at a single grazing angle, often at the isokinetic angle, defined as the critical angle of total external reflection divided by $\sqrt{2}$. The advantage of measurements at these angles is that grazing XRF techniques allow measurements unaffected by XRF or scattering background from the bulk volume of the substrate, while providing enhanced excitation (GIXRF) or detection (GEXRF) of the fluorescence radiation originating from the sample volume at the top of the refracting substrate interface. Note that for purely quantitative purposes, where no depth-profiling information is of interest, the requirements for monochromaticity (GIXRF) and collimation (GIXRF and GEXRF) of the grazing radiation can be relaxed somewhat, possibly lowering the detection limits and improving the statistics of the measurement itself.

Different quantification schemes can be used for quantification purposes: external calibration, internal standardization and reference-free measurements.[15] External standardization uses a set of reference samples, ideally characterized by other analytical approaches, to construct a calibration curve for each element of interest, whereas internal standardization uses a known amount of a standard that has no spectral overlap with the XRF lines of the elements of interest. In principle, the latter approach also requires homogenization with the sample material being investigated to account for locally varying excitation conditions, whereas the former approach requires samples that are representative of the sample type (in terms of depth distribution (layer, particle-like, implantation profile), surface coverage (if applicable) and elemental matrix) being investigated. The common idea is to obtain the necessary information to be able to transfer measured X-ray fluorescence counts into an elemental mass deposition. In reference-free measurements, the individual parts of the instrumentation is radiometrically calibrated to allow absolute measurements. The knowledge required includes, in combination or individually, the incident photon flux, the solid angle of detection, the detection efficiency and, depending on the evaluation strategy, the response function of the detector used. Once this information is available, the XRF count rate associated with an element can be converted to a mass deposition (number of atoms per unit area integrated over the depth direction). For internal standardization and the reference-free approach, knowledge of the fundamental atomic parameters is also required.

A potential problem with quantitative measurements in TXRF is that, regardless of the quantification routine used, the mass deposition determined is obtained from a single point measurement in the sense that measurements are realized at single grazing incidence angle. This means that it is important to ensure that external or internal calibration strategies are applied in a linear regime where the measured count rate and elemental mass deposition are linearly correlated. For external calibration, the linearity of the calibration curve can be assessed and non-linearity can even be accounted for within a certain range, provided that the calibration samples used cover a sufficiently wide range. The non-linearity results from the strong absorption of incident X-rays and fluorescence radiation within the sample volume, so that it can no longer be assumed that all analyte volumes contribute equally to the measured XRF count rate. This aspect is important when mass depositions are too high for classical XRF applications. The same statement applies to reference-free approaches, since the calculated X-ray standing wave field must be assumed to be correct, either by using tabulated reflectivity values and taking into account the presence of the analyte material to be investigated, or by using experimentally determined reflectivity of the samples used for the measurements.

These requirements can also be checked by controlled variation of the excitation parameters, one possibility being the grazing angle used in the measurements. In particular, by tuning the grazing angle to values above the critical angle of total external reflection, measurement conditions with and without refraction effects can be easily compared, as it is shown in Fig. 17. Since the elemental mass deposition does not change, the quantification results are expected to be independent of the grazing angle. This controlled variation of the experimental parameters can be used to confirm or falsify the quantification results. Note that for low mass depositions the increase in scattering background may render the angular regime above the critical angle of total external reflection unsuitable for such investigations, but in such cases a variation of the grazing angle in the angular regime below the critical angle of total external reflection may prove equally suitable.[202] The loss of volatile material during investigation of the samples in a high vacuum environment usually needs to be considered as well, but the stability of the quantification results at larger incidence angles (or also at grazing angles for samples with low
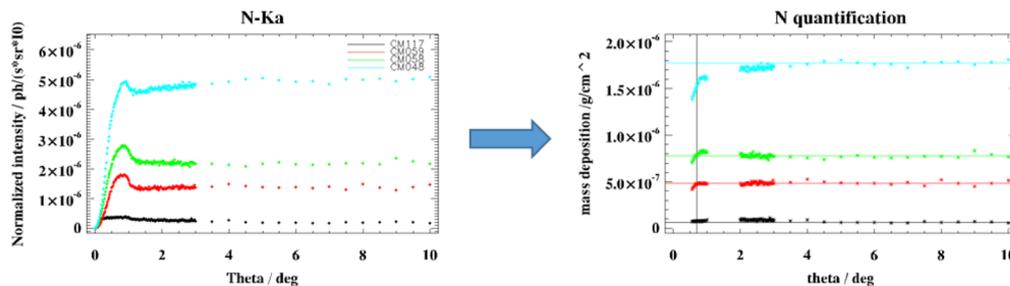
This journal is © The Royal Society of Chemistry 2025

J. Anal. At. Spectrom., 2025, **40**, 3368–3393 | **3383**

Fig. 17 GIXRF measurement on the N–K XRF lines of airborne particulate matter measured at 1.622 keV (left panel) and ensuing quantification at different grazing incidence angles (right panel), showing that with increasing mass deposition the results are not consistent with each other.

enough mass deposition) for all elements considered suggested that this issue was not a problem in the discussed investigation.

This self-consistent validation strategy for mass deposition quantification has been applied to samples from air quality monitoring campaigns, where varying concentrations and sampling times of airborne particulate matter (PM) result in a large dynamic range of mass deposition to be quantified by reference-free GIXRF.[202] By quantifying airborne PM at different angles of incidence, the self-consistency of the different experimental results could be verified and samples unsuitable for quantification under TXRF conditions could be identified.

5 Conclusion and future perspective

Grazing incidence X-ray fluorescence (GIXRF) and grazing incidence X-ray fluorescence (GEXRF) are essential tools for the comprehensive characterization of thin films and nanostructures and offer unique opportunities for elemental analysis and depth profiling while not facing the same limitations than electron or ion-based techniques in terms of required sample properties or measurement environment. This review explains the basic principles, theoretical framework and practical applications of these advanced X-ray techniques. Based on calculations of the X-ray standing wave field, both GIXRF and GEXRF enable non-destructive, depth-resolved investigations at the nanometer scale, providing crucial insights into material composition, film thickness and interface properties. The increasing accessibility of laboratory setups next to established synchrotron facilities underlines the growing importance of GIXRF and GEXRF in various technology areas and drives the development and analysis of nanomaterials.

In the future, the GIXRF and GEXRF methods will profit from further innovations in X-ray source technology, detector sensitivity and optical components. As in the past, this will further improve the spatial resolution, detection limits and measurement speed of these methods. The integration of advanced data analysis methods, including machine learning and artificial intelligence, will simplify complex data deconvolution and speed up the interpretation of results, making these powerful tools accessible to a wider range of researchers. Furthermore, their synergistic combination with other complementary characterization techniques will progress towards a more holistic understanding of complex nanomaterial systems and position

GIXRF and GEXRF as a crucial analytical technique at the forefront of nanoscale materials science and engineering.

Equally crucial, the continued exploration and identification of new application areas will further enhance the impact of these methods. As demonstrated in the context of semiconductor nanostructures, where precise control of dimensional and elemental composition is enabled non-destructively using GIXRF and GEXRF, the two methods still have much potential. In addition, these techniques are extremely promising for the characterization of complex materials in areas such as advanced catalysis by studying elemental distribution at active sites, environmental science for the analysis of nanoparticles and pollutants on surfaces, and energy materials research to understand degradation mechanisms in battery electrodes or photovoltaic devices. Expanding the range of applications will not only refine these techniques, but also open up new avenues for scientific discovery and technological innovation in various disciplines.

Author contributions

Y. Kayser: writing, reviewing, editing, conceptualization M. Krämer: writing, reviewing, editing P. Hönicke: writing, reviewing, editing, conceptualization, visualizations.

Conflicts of interest

There are no conflicts of interest to declare.

Data availability

No primary research results, software or code have been included and no new data were generated or analyzed as part of this review.

Acknowledgements

References

1 P. Wobrauschek, Total reflection x-ray fluorescence analysis - a review, *X Ray Spectrom.*, 2007, **36**(5), 289–300.

2 M. Schmeling, Total reflection X-ray fluorescence, *Phys. Sci. Rev.*, 2019, **4**(7), 20170161.

3 D. K. G. de Boer, Angular dependence of X-ray fluorescence intensities, *X-Ray Spectrom.*, 1989, **18**, 119–129.

4 W. W. Van Den Hoogenhof and D. K. G. De Boer, Glancing-incidence X-ray analysis, *Spectrochim. Acta, Part B*, 1993, **48**(2), 277–284. Available from: **https:// www.sciencedirect.com/science/article/pii/ 058485479380034R**.

5 D. K. G. de Boer, A. J. G. Leenaers and W. W. van den Hoogenhof, Glancing-incidence x-ray analysis of thin-layered materials: A review, *X-Ray Spectrom.*, 1995, **24**(3), 91–102.

6 K. N. Stoev and K. Sakurai, Review on grazing incidence X-ray spectrometry and reflectometry, *Spectrochim. Acta, Part B*, 1999, **54**, 41–82.

7 R. Klockenkämper and A. von Bohlen, *Total-Reflection X-Ray Fluorescence Analysis and Related Methods*, John Wiley & Sons, Inc., 2014.

8 R. S. Becker, J. A. Golovchenko and J. R. Patel, X-Ray Evanescent-Wave Absorption and Emission, *Phys. Rev. Lett.*, 1983, **50**(3), 153–156. Available from: **https:// link.aps.org/doi/10.1103/PhysRevLett.50.153**.

9 A. von Bohlen, Total reflection X-ray fluorescence and grazing incidence X-ray spectrometry—Tools for micro- and surface analysis. A review, *Spectrochim. Acta, Part B*, 2009, **64**(9), 821–832.

10 J. Baumann, Y. Kayser and B. Kanngießer, Grazing Emission X-Ray Fluorescence: Novel Concepts and Applications for Nano-Analytics, *Phys. Status Solidi B*, 2020, 2000471.

11 J. Sherman, The theoretical derivation of fluorescent X-ray intensities from mixtures, *Spectrochim Acta*, 1955, **7**, 283–306.

12 P. Hönicke, B. Beckhoff, M. Kolbe, D. Giubertoni, J. A. van den Berg and G. Pepponi, Depth profile characterization of ultra shallow junction implants, *Anal. Bioanal. Chem.*, 2010, **396**(8), 2825–2832.

13 P. Hönicke, B. Detlefs, E. Nolot, Y. Kayser, U. Mühle, B. Pollakowski, *et al.*, Reference-free grazing incidence X-ray fluorescence and reflectometry as a methodology for independent validation of X-ray reflectometry on ultrathin layer stacks and a depth-dependent characterization, *J. Vac. Sci. Technol., A*, 2019, **37**(4), 041502.

14 P. Hönicke, U. Waldschläger, T. Wiesner, M. Krämer and B. Beckhoff, Towards a calibration of laboratory setups for grazing incidence and total-reflection X-ray fluorescence analysis, *Spectrochim. Acta, Part B*, 2020, **174**, 106009.

15 B. Beckhoff, R. Fliegauf, M. Kolbe, M. Müller, J. Weser and G. Ulm, Reference-Free Total Reflection X-ray Fluorescence Analysis of Semiconductor Surfaces with Synchrotron Radiation, *Anal. Chem.*, 2007, **79**, 7873–7882.

16 W. Li, J. Zhu, X. Ma, H. LI, H. Wang, K. J. S. Sawhney, *et al.*, Geometrical factor correction in grazing incident x-ray fluorescence experiment, *Rev. Sci. Instrum.*, 2012, **83**, 053114.

17 D. Ingerle, G. Pepponi, F. Meirer, P. Wobrauschek and C. Streli, JGIXA — A software package for the calculation and fitting of grazing incidence X-ray fluorescence and X-ray reflectivity data for the characterization of nanometer-layers and ultra-shallow-implants, *Spectrochim. Acta, Part B*, 2016, **118**, 20–28. Available from: **https:// www.sciencedirect.com/science/article/pii/ S0584854716300015**.

18 P. Hönicke, A. Andrle, Y. Kayser, K. V. Nikolaev, J. Probst, F. Scholze, *et al.*, Grazing incidence-x-ray fluorescence for a dimensional and compositional characterization of well-ordered 2D and 3D nanostructures, *Nanotechnology*, 2020, **31**(50), 505709, DOI: **10.1088/1361-6528/abb557**.

19 S. Melhem, Y. Ménesguen, E. Nolot and M. C. Lépy, A step toward calculating the uncertainties in combined GIXRF-XRR, *X-Ray Spectrom.*, 2023, **52**(6), 412–422.

20 L. G. Parratt, Surface Studies of Solids by Total Reflection of X-Rays, *Phys. Rev.*, 1954, **95**(2), 359–369.

21 D. K. G. de Boer, Glancing-incidence X-ray fluorescence of layered materials, *Phys. Rev. B: Condens. Matter Mater. Phys.*, 1991, **44**(2), 498–511.

22 D. L. Windt, IMD—Software for modeling the optical properties of multilayer films, *Comput. Phys.*, 1998, **12**(4), 360–370.

23 M. K. Tiwari, G. S. Lodha and K. J. S. Sawhney, Applications of the 'CATGIXRF' computer program to the grazing incidence X-ray fluorescence and X-ray reflectivity characterization of thin films and surfaces, *X-Ray Spectrom.*, 2010, **39**(2), 127–134. Available from: **https:// analyticalsciencejournals.onlinelibrary.wiley.com/doi/abs/ 10.1002/xrs.1215**.

24 M. Krämer, A. von Bohlen, C. Sternemann, M. Paulus and R. Hergenröder, X-ray standing waves: a method for thin layered systems, *J. Anal. At. Spectrom.*, 2006, **21**, 1136–1142, DOI: **10.1039/B607252F**.

25 F. Brigidi and G. Pepponi, GIMPy: a software for the simulation of X-ray fluorescence and reflectivity of layered materials, *X Ray Spectrom.*, 2017, **46**(2), 116–122.

26 P. Hönicke, Y. Kayser, B. Beckhoff, M. Müller, J. C. Dousse, J. Hoszowska, *et al.*, Characterization of ultra shallow aluminum implants in silicon by grazing incidence and grazing emission X-ray fluorescence spectroscopy, *J. Anal. At. Spectrom.*, 2012, **27**, 1432–1438.

27 D. Ingerle, M. Schiebl, C. Streli and P. Wobrauschek, Combination of grazing incidence x-ray fluorescence with x-ray reflectivity in one table-top spectrometer for

This journal is © The Royal Society of Chemistry 2025

J. Anal. At. Spectrom., 2025, **40**, 3368–3393 | **3385**

improved characterization of thin layer and implants on/in silicon wafers, *Rev. Sci. Instrum.*, 2014, **85**, 083110.

28 S. Kim, G. Kioseoglou, S. Huang, Y. H. Kao, Y. L. Soo, X. Zhu, *et al.*, Characterization of nanostructure in $Si_{1-x}Ge_x$ epilayers using x-ray reflectivity and fluorescence techniques, *J. Appl. Phys.*, 2005, **98**, 074309.

29 E. Arac, D. M. Burn, D. S. Eastwood, T. P. A. Hase and D. Atkinson, Study of focused-ion-beam–induced structural and compositional modifications in nanoscale bilayer systems by combined grazing incidence x ray reflectivity and fluorescence, *J. Appl. Phys.*, 2012, **111**, 044324.

30 X. Yang, W. Li, J. Zhu, X. Li and Z. Wang, Structural characterization of multilayer using the analysis combining GIXRF with GIXRR method, *Proc. SPIE*, 2013, **9068**, 90680X.

31 A. Lesnik, J. Bläsing, J. Hennig, A. Dadgar and A. Krost, Characterization of AlInN/AlN/GaN FET structures using x-ray diffraction, x-ray reflectometry and grazing incidence x-ray fluorescence analysis, *J. Phys. D: Appl. Phys.*, 2014, **47**(35), 355106.

32 B. Caby, F. Brigidi, D. Ingerle, E. Nolot, G. Pepponi, C. Streli, *et al.*, Study of annealing induced inter diffusion in In_2O_3/ Ag/In_2O_3 structures by a combined X-ray reflectivity and grazing incidence X-ray fluorescence analysis, *Spectrochim. Acta, Part B*, 2015, **113**, 132–137.

33 H. Rotella, B. Caby, Y. Ménesguen, Y. Mazel, A. Valla, D. Ingerle, *et al.*, Elemental depth profiling in transparent conducting oxide thin film by X-ray reflectivity and grazing incidence X-ray fluorescence combined analysis, *Spectrochim. Acta, Part B*, 2017, **135**, 22–28.

34 E. Nolot, B. Caby, R. Gassilloud, M. Veillerot and D. Eichert, X-ray reflectometry and grazing-incidence X-ray fluorescence characterization of innovative electrodes for tantalum-based resistive random access memories, *Spectrochim. Acta, Part B*, 2018, **149**, 71–75.

35 A. Maderitsch, D. Ingerle, T. Bretschneider, M. Rauwolf, C. Pflumm, H. Buchholz, *et al.*, Analysis of organic multilayer structures using a combined grazing incidence X-ray fluorescence/X-ray reflectometry approach, *Spectrochim. Acta, Part B*, 2018, **148**, 188–192.

36 W. Pessoa, A. Roule, E. Nolot, Y. Mazel, M. Bernard, M. C. Lépy, *et al.*, Grazing incident X-ray fluorescence combined with X-ray reflectometry metrology protocol of telluride-based films using in-lab and synchrotron instruments, *Spectrochim. Acta, Part B*, 2018, **149**, 143–149.

37 D. R. Kiranjot and M. H. Modi, Surface and interface characterization of Ru/C/Ru trilayer structure using grazing incidence X-ray reflectivity and X-ray fluorescence, *Surf. Interface Anal.*, 2021, **54**(1), 52–58.

38 I. A. Makhotkin, E. Louis, R. W. E. van de Kruijs, A. E. Yakshin, E. Zoethout, A. Y. Seregin, *et al.*, Determination of the density of ultrathin La films in La/ B4C layered structures using X-ray standing waves, *Phys. Status Solidi*, 2011, **208**(11), 2597–2600.

39 S. N. Yakunin, I. A. Makhotkin, R. W. E. van de Kruijs, M. A. Chuev, E. M. Pashaev, E. Zoethout, *et al.*, Model

independent x-ray standing wave analysis of periodic multilayer structures, *J. Appl. Phys.*, 2014, **115**, 134303.

40 G. Das, S. R. Kane, A. Khooha, A. K. Singh and M. K. Tiwari, Simultaneous measurements of X-ray reflectivity and grazing incidence fluorescence at BL-16 beamline of Indus-2, *Rev. Sci. Instrum.*, 2015, **86**, 055102.

41 G. Das, A. Khooha, A. K. Singh, A. K. Srivastava and M. K. Tiwari, Exploring interface morphology of a deeply buried layer in periodic multilayer, *Appl. Phys. Lett.*, 2016, **108**, 263109.

42 P. Jonnard, K. L. Guen, R. Delaunay, Y. Ménesguen, M. C. Lépy, E. Briand, *et al.*, Combined x-ray reflectivity and grazing incidence x-ray fluorescence study of Ta/Cr/Pt thin film stacks, *X-Ray Spectrom.*, 2023, **52**(6), 437–446.

43 E. Nolot, W. Pessoa, S. Torrengo, Y. Mazel, M. Bernard, P. Gergaud, *et al.*, Grazing-incidence X-ray fluorescence analysis of thin chalcogenide materials deposited on Bragg mirrors, *Spectrochim. Acta, Part B*, 2020, **168**, 105864.

44 D. Ingerle, F. Meirer, G. Pepponi, E. Demenev, D. Giubertoni, P. Wobrauschek, *et al.*, Combined evaluation of grazing incidence x-ray fluorescence and x-ray reflectivity data for improved profiling of ultra-shallow depth distributions, *Spectrochim. Acta, Part B*, 2014, **99**, 121–128.

45 Y. Choi, P. Eng, J. Stubbs, S. R. Sutton, M. Schmeling, I. V. Veryovkin, *et al.*, Discrimination and quantification of Fe and Ni abundances in genesis solar wind implanted collectors using X-ray standing wave fluorescence yield depth profiling with internal referencing, *Chem. Geol.*, 2016, **441**, 246–255.

46 A. Trivedi, P. N. Rao, R. J. Choudhary and M. K. Tiwari, Determination of arsenic diffusion in PLD grown ZnO thin films using synchrotron based XRR-GIXRF measurements, *AIP Conf. Proc.*, 2019, **2115**, 030315.

47 H. H. Radamson, X. He, Q. Zhang, J. Liu, H. Cui, J. Xiang, *et al.*, Miniaturization of CMOS, *Micromachines*, 2019, **10**(5), 293.

48 F. Reinhardt, S. H. Nowak, B. Beckhoff, J. C. Dousse and M. Schoengen, Grazing Incidence X-ray Fluorescence of periodic structures – a comparison between X-ray Standing Waves and Geometrical Optics calculations, *J. Anal. At. Spectrom.*, 2014, **29**, 1778–1784.

49 V. Soltwisch, P. Hönicke, Y. Kayser, J. Eilbracht, J. Probst, F. Scholze, *et al.*, Element sensitive reconstruction of nanostructured surfaces with finite-elements and grazing incidence soft X-ray fluorescence, *Nanoscale*, 2018, **10**, 6177–6185.

50 P. Hönicke, A. Andrle, Y. Kayser, K. V. Nikolaev, J. Probst, F. Scholze, *et al.*, Grazing incidence-X-ray fluorescence for a dimensional and compositional characterization of well-ordered 2D and 3D nanostructures, *Nanotechnology*, 2020, **31**(50), 505709.

51 P. Hönicke, Y. Kayser, K. V. Nikolaev, V. Soltwisch, J. E. Scheerder, C. Fleischmann, *et al.*, Simultaneous Dimensional and Analytical Characterization of Ordered Nanostructures, *Small*, 2022, **18**(6), 2105776. Available

3386 | *J. Anal. At. Spectrom.*, 2025, **40**, 3368–3393

This journal is © The Royal Society of Chemistry 2025

from: https://onlinelibrary.wiley.com/doi/abs/10.1002/smll.202105776.

52 H. Kiessig, Interferenz von Röntgenstrahlen an dünnen Schichten, *Ann. Phys.*, 1931, **402**(7), 769–788.

53 J. Lubeck, B. Beckhoff, R. Fliegauf, I. Holfelder, P. Hönicke, M. Müller, *et al.*, A novel instrument for quantitative nanoanalytics involving complementary X-ray methodologies, *Rev. Sci. Instrum.*, 2013, **84**, 045106.

54 Y. Ménesguen, B. Boyer, H. Rotella, J. Lubeck, J. Weser, B. Beckhoff, *et al.*, CASTOR, a new instrument for combined XRR-GIXRF analysis at SOLEIL, *X-Ray Spectrom.*, 2017, **46**(5), 303–308. Available from: https://analyticalsciencejournals.onlinelibrary.wiley.com/doi/abs/10.1002/xrs.2742.

55 M. Paulus, D. Lietz, C. Sternemann, K. Shokuie, F. Evers, M. Tolan, *et al.*, An access to buried interfaces: the X-ray reflectivity set-up of BL9 at DELTA, *J. Synchrotron Radiat.*, 2008, **15**(6), 600–605.

56 A. G. Karydas, M. Czyzycki, J. J. Leani, A. Migliori, J. Osan, M. Bogovac, *et al.*, An IAEA multi-technique X-ray spectrometry endstation at Elettra Sincrotrone Trieste: benchmarking results and interdisciplinary applications, *J. Synchrotron Radiat.*, 2018, **25**(1), 189–203.

57 D. Ingerle, F. Meirer, N. Zoeger, G. Pepponi, D. Giubertoni, G. Steinhauser, *et al.*, A new spectrometer for grazing incidence X-ray fluorescence for the characterization of Arsenic implants and Hf based high-k layers, *Spectrochim. Acta, Part B*, 2010, **65**(6), 429–433.

58 L. Borgese, M. Salmistraro, A. Gianoncelli, A. Zacco, R. Lucchini, N. Zimmerman, *et al.*, Airborne particulate matter (PM) filter analysis and modeling by total reflection X-ray fluorescence (TXRF) and X-ray standing wave (XSW), *Talanta*, 2012, **89**, 99–104.

59 V. Szwedowski-Rammert, J. Baumann, C. Schlesiger, U. Waldschlaeger, A. Gross, B. Kanngießer, *et al.*, Laboratory based GIXRF and GEXRF spectrometers for multilayer investigations, *J. Anal. At. Spectrom.*, 2019, **34**(5), 922–929.

60 D. Ingerle, W. Artner, K. Hradil and C. Streli, Refitting an X-ray diffraction system for combined GIXRF and XRR measurements, *Powder Diffr.*, 2020, 1–5.

61 V. Szwedowski-Rammert, P. Hönicke, M. Wu, U. Waldschläger, A. Gross, J. Baumann, *et al.*, Laboratory grazing-incidence X-ray fluorescence spectroscopy as an analytical tool for the investigation of sub-nanometer CrSc multilayer water window optics, *Spectrochim. Acta, Part B*, 2020, **174**, 105995.

62 D. K. G. de Boer, Glancing-incidence x-ray fluorescence of layered materials, *Phys. Rev. B: Condens. Matter Mater. Phys.*, 1991, **44**(2), 498–511.

63 H. P. Urbach and P. K. de Bokx, Calculation of intensities in grazing-emission x-ray fluorescence, *Phys. Rev. B: Condens. Matter Mater. Phys.*, 1996, **53**(7), 3752–3763.

64 H. P. Urbach and P. K. de Bokx, Grazing emission x-ray fluorescence from multilayers, *Phys. Rev. B: Condens. Matter Mater. Phys.*, 2001, **63**(8), 085408.

65 Y. Kayser, J. Szlachetko, D. Banaś, W. Cao, J. C. Dousse, J. Hoszowska, *et al.*, High-energy-resolution grazing emission X-ray fluorescence applied to the characterization of thin Al films on Si, *Spectrochim. Acta, Part B*, 2013, **88**, 136–149. Available from: http://www.sciencedirect.com/science/article/pii/S0584854713001663.

66 M. Claes, P. de Bokx and R. van Grieken, Progress in laboratory grazing emission X-ray fluorescence spectrometry, *X-Ray Spectrom.*, 1999, **28**(4), 224–229.

67 P. K. de Bokx, C. Kok, A. Bailleul, G. Wiener and H. P. Urbach, Grazing-emission X-ray fluorescence spectrometry; principles and applications, *Spectrochim. Acta, Part B*, 1997, **52**(7), 829–840.

68 P. K. de Bokx and H. P. Urbach, Laboratory grazing-emission x-ray fluorescence spectrometer, *Rev. Sci. Instrum.*, 1995, **66**(1), 15.

69 V. Szwedowski, J. Baumann, I. Mantouvalou, L. Bauer, W. Malzer and B. Kanngießer, Scan-Free Grazing Emission XRF Measurements in the Laboratory Using a CCD, *Phys. Status Solidi C*, 2017, **14**(12), 1700158.

70 Y. Suzuki, Surface extended X-ray-absorption fine-structure spectroscopy measurement using the evanescent-wave effect of fluorescent X-ray, *Phys. Rev. B: Condens. Matter Mater. Phys.*, 1989, **39**(5), 3393–3395.

71 T. Noma, A. Iida and K. Sakurai, Fluorescent-x-ray-interference effect in layered materials, *Phys. Rev. B: Condens. Matter Mater. Phys.*, 1993, **48**(23), 17524–17526.

72 Y. Kayser, D. Banaś, W. Cao, J. C. Dousse, J. Hoszowska, P. Jagodziński, *et al.*, Depth profiling of dopants implanted in Si using the synchrotron radiation based high-resolution grazing emission technique, *X-Ray Spectrom.*, 2012, **41**(2), 98–104.

73 H. Schwenke, J. Knoth, P. A. Beaven, R. Kiehn and J. Buhrz, A laser plasma X-ray source for the analysis of wafer surfaces by grazing emission X-ray fluorescence spectrometry, *Spectrochim. Acta, Part B*, 2004, **59**(8), 1159–1164.

74 J. Baumann, C. Herzog, M. Spanier, D. Grötzsch, L. Lühl, K. Witte, *et al.*, Laboratory Setup for Scanning-Free Grazing Emission X-ray Fluorescence, *Anal. Chem.*, 2017, **89**(3), 1965–1971.

75 K. Tsuji, Grazing-exit electron probe X-ray microanalysis (GE-EPMA): Fundamental and applications, *Spectrochim. Acta, Part B*, 2005, **60**(11), 1381–1391.

76 Z. Spolnik, K. Tsuji and R. van Grieken, Grazing-exit electron probe x-ray microanalysis of light elements in particles, *X-Ray Spectrom.*, 2004, **33**(1), 16–20.

77 K. Tsuji, Z. Spolnik, K. Wagatsuma, G. Van, E. René and R. D. Vis, Grazing-Exit Particle-Induced X-ray Emission Analysis with Extremely Low Background, *Anal. Chem.*, 1999, **71**(22), 5033–5036.

78 J. Miranda, J. Rickards and R. Trejo-Luna, PIXE depth profiling using variation of detection angle, *Nucl. Instrum. Methods Phys. Res., Sect. B*, 2006, **249**(1–2), 394–396.

79 C. Kok and H. P. Urbach, On the regularization of the inverse laplace transform in grazing-emission X-ray

This journal is © The Royal Society of Chemistry 2025

J. Anal. At. Spectrom., 2025, **40**, 3368–3393 | **3387**

fluorescence spectroscopy, *Inverse Probl. Eng.*, 1999, **7**(5), 433–470.

80 K. Tsuji, H. Takenaka, K. Wagatsuma, P. K. de Bokx, G. Van and E. René, Enhancement of X-ray fluorescence intensity from an ultra-thin sandwiched layer at grazing-emission angles, *Spectrochim. Acta, Part B*, 1999, **54**(13), 1881–1888.

81 A. Kuczumow, M. Schmeling and R. van Grieken, Critical assessment and proposal for reconstruction of a grazing emission X-ray fluorescence instrument, *J. Anal. At. Spectrom.*, 2000, **15**(5), 535–542.

82 N. Awaji, Wavelength dispersive grazing incidence X-ray fluorescence of multilayer thin films, *Spectrochim. Acta, Part B*, 2004, **59**(8), 1133–1139. 10th Symposium on Total Reflection X-Ray Fluorescence Analysis and 39th Discussion Meeting on Chemical Analysis. Available from: **https://www.sciencedirect.com/science/article/pii/S0584854704001120**.

83 Y. Kayser, P. Hönicke, D. Banaś, J. C. Dousse, J. Hoszowska, P. Jagodziński, *et al.*, Depth profiling of low energy ion implantations in Si and Ge by means of micro-focused grazing emission X-ray fluorescence and grazing incidence X-ray fluorescence, *J. Anal. At. Spectrom.*, 2015, **30**(5), 1086–1099.

84 Y. Kayser, J. Szlachetko and J. Sà, Scanning-free grazing emission x-ray fluorescence by means of an angular dispersive arrangement with a two-dimensional position-sensitive area detector, *Rev. Sci. Instrum.*, 2013, **84**(12), 123102.

85 V. Szwedowski-Rammert, J. Baumann, C. Schlesiger, U. Waldschläger, A. Gross, B. Kanngießer, *et al.*, Laboratory based GIXRF and GEXRF spectrometers for multilayer structure investigations, *J. Anal. At. Spectrom.*, 2019, **34**(5), 922–929, DOI: **10.1039/C8JA00427G**.

86 S. Staeck, A. Andrle, P. Hönicke, J. Baumann, D. Grötzsch, J. Weser, *et al.*, Scan-Free GEXRF in the Soft X-ray Range for the Investigation of Structured Nanosamples, *Nanomaterials*, 2022, **12**(21), 3766. Available from: **https://www.mdpi.com/2079-4991/12/21/3766**.

87 C. T. Cakir, T. Piotrowiak, U. Reinholz, A. Ludwig, F. Emmerling, C. Streli, *et al.*, Exploring the Depths of Corrosion: A Novel GE-XANES Technique for Investigating Compositionally Complex Alloys, *Anal. Chem.*, 2023, **95**(10), 4810–4818, DOI: **10.1021/acs.analchem.3c00404**.

88 J. Szlachetko, D. Banaś, A. Kubala-Kukuś, M. Pajek, W. Cao, J. C. Dousse, *et al.*, Application of the high-resolution grazing-emission X-ray fluorescence method for impurities control in semiconductor nanotechnology, *J. Appl. Phys.*, 2009, **105**(8), 086101. Available from: **http://link.aip.org/link/?JAP/105/086101/1**.

89 B. L. Henke, E. M. Gullikson and J. C. Davis, X-ray interactions: photoabsorption, scattering, transmission, and reflection at E=50-30000 eV, Z=1-92, *At. Data Nucl. Data Tables*, 1993, **54**(2), 181–342.

90 R. D. Pérez and H. J. Sánchez, New spectrometer for grazing exit x-ray fluorescence, *Rev. Sci. Instrum.*, 1997, **68**(7), 2681–2684.

91 F. Meirer, A. Singh, P. Pianetta, G. Pepponi, C. Streli and T. Homma, Synchrotron radiation-induced total reflection X-ray fluorescence analysis, *TrAC, Trends Anal. Chem.*, 2010, **29**(6), 479–496.

92 S. Sasaki and F. Tomioka, Observation of an interference effect for fluorescent x rays, *Phys. Rev. B: Condens. Matter*, 1993, **48**(10), 7724–7726.

93 D. Skroblin, A. Fernández Herrero, T. Siefke, K. Nikolaev, A. Andrle, P. Hönicke, *et al.*, Challenges of grazing emission X-ray fluorescence (GEXRF) for the characterization of advanced nanostructured surfaces, *Nanoscale*, 2022, **14**, 15475–15483, DOI: **10.1039/D2NR03046B**.

94 F. P. Romano, C. Caliri, L. Cosentino, S. Gammino, L. Giuntini, D. Mascali, *et al.*, Macro and micro full field x-ray fluorescence with an X-ray pinhole camera presenting high energy and high spatial resolution, *Anal. Chem.*, 2014, **86**(21), 10892–10899.

95 J. Baumann, R. Gnewkow, S. Staeck, V. Szwedowski-Rammert, C. Schlesiger, I. Mantouvalou, *et al.*, Photon event evaluation for conventional pixelated detectors in energy-dispersive X-ray applications, *J. Anal. At. Spectrom.*, 2018, **33**(12), 2043–2052.

96 O. Scharf, S. Ihle, I. Ordavo, V. Arkadiev, A. Bjeoumikhov, S. Bjeoumikhova, *et al.*, Compact pnCCD-based X-ray camera with high spatial and energy resolution: a color X-ray camera, *Anal. Chem.*, 2011, **83**(7), 2532–2538.

97 J. Baumann, D. Grötzsch, O. Scharf, T. Kodalle, R. Bergmann, F. Bilchenko, *et al.*, A compact and efficient angle-resolved X-ray fluorescence spectrometer for elemental depth profiling, *Spectrochim. Acta, Part B*, 2021, **181**, 106216. Available from: **https://www.sciencedirect.com/science/article/pii/S0584854721001737**.

98 K. Desjardins, H. Popescu, P. Mercère, C. Menneglier, R. Gaudemer, K. Thånell, *et al.*, Characterization of a back-illuminated CMOS camera for soft x-ray coherent scattering, In: *AIP Conf. Proc. 2054*, AIP Publishing, 2019, p. 060066.

99 W. X. Wang, Z. X. Ling, C. Zhang, Z. Q. Jia, X. Y. Wang, Q. Wu, *et al.*, Characterization of a BSI sCMOS for soft X-ray imaging spectroscopy, *J. Instrum.*, 2019, **14**(02), P02025.

100 T. Harada, N. Teranishi, T. Watanabe, Q. Zhou, J. Bogaerts and X. Wang, High-exposure-durability, high-quantum-efficiency (>90%) backside-illuminated soft-X-ray CMOS sensor, *Appl. Phys. Express*, 2020, **13**(1), 016502.

101 S. Staeck, Y. Kayser, J. Baumann, A. Jonas, I. Mantouvalou, R. Hartmann, *et al.*, Towards soft x-ray fluorescence measurements in the laboratory using a laser-produced plasma source and a complementary metal-oxide semiconductor detector, *J. Instrum.*, 2021, **16**(03), P03033, DOI: **10.1088/1748-0221/16/03/P03033**.

102 P. Skytt, B. Galnander, T. Nyberg, J. Nordgren and P. Isberg, Probe depth variation in grazing exit soft-X-ray emission spectroscopy, *Nucl. Instrum. Methods Phys. Res. Sect. A Accel. Spectrom. Detect. Assoc. Equip.*, 1997, **384**(2–3), 558–562. Available from: **http://www.sciencedirect.com/**

science/article/B6TJM-3SPCMY9-30/2/c645db264c3bde2d3a8792fb70ac89ab.

103 S. H. Nowak, D. Banaś, W. Blchucki, W. Cao, J. C. Dousse, P. Hönicke, *et al.*, Grazing angle X-ray fluorescence from periodic structures on silicon and silica surfaces, *Spectrochim. Acta, Part B*, 2014, **98**, 65–75.

104 K. Tsuji, S. Sato and K. Hirokawa, Depth profiling using the glancing–incidence and glancing–takeoff x-ray fluorescence method, *Rev. Sci. Instrum.*, 1995, **66**(10), 4847–4852. Available from: http://link.aip.org/link/?RSI/66/4847/1.

105 S. Sato, K. Tsuji and K. Hirokawa, Evaluation of Ni/Mn multilayer samples with glancing-incidence and take-off X-ray fluorescence analysis, *Appl. Phys. A*, 1996, **62**, 87–93, DOI: 10.1007/BF01575706.

106 Y. C. Sasaki and K. Hirokawa, Refraction effect of scattered X-ray fluorescence at surface, *Appl. Phys. A*, 1990, **50**(4), 397–404.

107 K. Tsuji, S. Sato and K. Hirokawa, Glancing-incidence and glancing-takeoff X-ray fluorescence analysis of a Mn ultrathin film on an Au layer, *Thin Solid Films*, 1996, **274**(1–2), 18–22.

108 K. Tsuji, K. Wagatsuma and T. Oku, Glancing-incidence and glancing-takeoff x-ray fluorescence analysis of Ni-GaAs interface reactions, *X-Ray Spectrom.*, 2000, **29**(2), 155–160.

109 S. M. George, Atomic Layer Deposition: An Overview, *Chem. Rev.*, 2010, **110**(1), 111–131, DOI: 10.1021/cr900056b.

110 L. Sun, G. Yuan, L. Gao, J. Yang, M. Chhowalla, M. H. Gharahcheshmeh, *et al.*, Chemical vapour deposition, *Nat. Rev. Methods Primers*, 2021, **1**, 5, DOI: 10.1038/s43586-020-00005-y.

111 M. Krämer, A. von Bohlen, C. Sternemann, M. Paulus and R. Hergenröder, Synchrotron radiation induced X-ray standing waves analysis of layered structures, *Appl. Surf. Sci.*, 2007, **253**(7), 3533–3542.

112 M. K. Tiwari and K. J. S. Sawhney, Structural characterization of thin layered materials using x-ray standing wave enhanced elastic and inelastic scattering measurements, *J. Phys.*, 2010, **22**, 175003.

113 A. Gupta, D. Kumar and V. Phat, Asymmetric diffusion at the interfaces in Fe/Si multilayers, *Phys. Rev. B: Condens. Matter Mater. Phys.*, 2010, **81**, 155402.

114 H. J. Sánchez and C. A. Pérez, Study of copper surface oxidation by grazing angle X-ray excitation, *Spectrochim. Acta, Part B*, 2010, **65**(6), 466–470.

115 M. Brücher, P. Jacob, A. von Bohlen, J. Franzke, C. Sternemann, M. Paulus, *et al.*, Analysis of the Ion Distribution at a Charged Solid-Liquid Interface Using X-ray Standing Waves, *Langmuir*, 2010, **26**(2), 959–966.

116 E. Schneck, T. Schubert, O. V. Konovalov, B. E. Quinn, T. Gutsmann, K. Brandenburg, *et al.*, Quantitative determination of ion distributions in bacterial lipopolysaccharide membranes by grazing-incidence X-ray fluorescence, *Proc. Natl. Acad. Sci. U. S. A.*, 2010, **107**(20), 9147–9151.

117 R. Unterumsberger, B. Pollakowski, M. Müller and B. Beckhoff, Complementary Characterization of Buried Nanolayers by Quantitative X-ray Fluorescence Spectrometry under Conventional and Grazing Incidence Conditions, *Anal. Chem.*, 2011, **83**(22), 8623–8628, DOI: 10.1021/ac202074s.

118 W. Li, J. Zhu, H. Li, Z. Zhang, X. Ma, X. Yang, *et al.*, Ni Layer Thickness Dependence of the Interface Structures for Ti/Ni/Ti Trilayer Studied by X-ray Standing Waves, *Appl. Mater. Interfaces*, 2013, **5**(2), 404–409.

119 S. Torrengo, D. Eichert, Y. Mazel, M. Bernard, Y. Ménesguen, M. C. Lépy, *et al.*, Quantitative depth-profile analysis of transition metal nitride materials with combined grazing-incidence X-ray fluorescence and X-ray reflectometry analysis, *Spectrochim. Acta, Part B*, 2020, **171**, 105926.

120 D. IJpes, A. E. Yakshin, J. M. Sturm and M. D. Ackermann, Increasing soft x-ray reflectance of short-period W/Si multilayers using B4C diffusion barriers, *J. Appl. Phys.*, 2023, **133**(2), 025302.

121 A. Trivedi, M. A. Alam, A. Khooha, R. Dhawan, R. K. Sharma, S. Tripathi, *et al.*, X-ray standing wave assisted XANES for depth dependent chemical state analysis of Cr in Cr2O3/Cr bilayer structure, *Surf. Interface Anal.*, 2024, **56**(11), 760–769.

122 K. V. Nikolaev, L. R. Muftakhova, G. M. Kuz'micheva, Y. N. Malakhova, A. V. Rogachev, N. N. Novikova, *et al.*, Probing Langmuir monolayer self-assembly in condensed and collapsed phases: grazing-incidence X-ray diffraction and X-ray standing wave studies, *J. Appl. Crystallogr.*, 2025, **58**(3), 696–710.

123 E. Cara, P. Hönicke, Y. Kayser, B. Beckhoff, A. M. Giovannozzi, P. Klapetek, *et al.*, Molecular surface coverage standards by reference-free GIXRF supporting SERS and SEIRA substrate benchmarking, *Nanophotonics*, 2024, **13**(25), 4605–4614.

124 A. Zoccante, E. Cara, F. Ferrarese Lupi, P. Hönicke, Y. Kayser, B. Beckhoff, *et al.*, The thermodynamics of self-assembled monolayer formation: a computational and experimental study of thiols on a flat gold surface, *Phys. Chem. Chem. Phys.*, 2024, **26**(27), 18799–18807.

125 P. Sarkar, A. Biswas, S. Rai, M. H. Modi, G. Ghorai, P. K. Sahoo, *et al.*, Impact of B4C buffer layer on interface diffusion in Cr/Sc multilayers: combined study by x-ray reflectivity, scattering and fluorescence, *Phys. Scr.*, 2024, **99**(6), 065952, DOI: 10.1088/1402-4896/ad451f.

126 I. Koshelev, A. Paulikas, M. Beno, G. Jennings, J. Linton, M. Grimsditch, *et al.*, Chromium–oxide Growth on Fe–Ni–Cr Alloy Studied with Grazing-emission X–ray Fluorescence, *Oxid. Met.*, 2007, **68**(15), 37–51.

127 M. L. Monaghan, T. Nigam, M. Houssa, S. D. Gendt, H. P. Urbach and P. K. de Bokx, Characterization of silicon oxynitride films by grazing-emission X-ray fluorescence spectrometry, *Thin Solid Films*, 2000, **359**(2), 197–202.

128 K. Tsuji, H. Takenaka, K. Wagatsuma, P. K. de Bokx and R. Van Grieken, Enhancement of X-ray fluorescence

This journal is © The Royal Society of Chemistry 2025

J. Anal. At. Spectrom., 2025, **40**, 3368–3393 | **3389**

intensity from an ultra-thin sandwiched layer at grazing-emission angles, *Spectrochim. Acta, Part B*, 1999, **54**(13), 1881–1888.

129 G. Wiener, S. J. Kidd, C. A. H. Mutsaers, R. A. M. Wolters and P. K. de Bokx, Characterization of titanium nitride layers by grazing-emission X-ray fluorescence spectrometry, *Appl. Surf. Sci.*, 1998, **125**(2), 129–136.

130 T. Noma, A. Iida and K. Sakurai, Fluorescent-x-ray-interference effect in layered materials, *Phys. Rev. B: Condens. Matter Mater. Phys.*, 1993, **48**(23), 17524–17526.

131 R. D. Pérez, H. J. Sánchez and M. Rubio, Theoretical model for the calculation of interference effects in TXRF and GEXRF, *X-Ray Spectrom.*, 2001, **30**(5), 292–295.

132 R. D. Pérez, H. J. Sánchez and M. Rubio, Efficient calculation method for glancing angle X-ray techniques, *X-Ray Spectrom.*, 2002, **31**(4), 296–299.

133 H. Schwenke, R. Gutschke, J. Knoth and M. Kock, Treatment of roughness and concentration gradients in total Reflection X-ray fluorescence analysis of surfaces, *Appl. Phys. A Mater. Sci. Process.*, 1992, **54**, 460–465.

134 K. Tsuji, T. Yamada, T. Utaka and K. Hirokawa, The effects of surface roughness on the angle-dependent total-reflection X-ray fluorescence of ultrathin films, *J. Appl. Phys.*, 1995, **78**(2), 969–973.

135 D. K. G. de Boer, X-ray scattering and x-ray fluorescence from materials with rough interfaces, *Phys. Rev. B: Condens. Matter Mater. Phys.*, 1996, **53**, 6048–6064. Available from: **https://link.aps.org/doi/10.1103/PhysRevB.53.6048**.

136 A. von Bohlen, Total reflection X-ray fluorescence and grazing incidence X-ray spectrometry – Tools for micro- and surface analysis. A review, *Spectrochim. Acta, Part B*, 2009, **64**(9), 821–832.

137 F. Meirer, A. Singh, P. Pianetta, G. Pepponi, F. Meirer, C. Streli, *et al.*, Synchrotron radiation–induced total reflection X–ray fluorescence analysis, *TrAC, Trends Anal. Chem.*, 2010, **29**(6), 479–496.

138 L. Bennun, Non linear effects in TXRF spectroscopy. A procedure for the evaluation of the dead time, *Spectrochim. Acta, Part B*, 2023, **203**, 106652. Available from: **https://www.sciencedirect.com/science/article/pii/S0584854723000393**.

139 G. Das, A. Khooha, A. K. Singh and M. K. Tiwari, Probing nanostructured materials using X-ray fluorescence analysis, *X-Ray Spectrom.*, 2017, **46**(5), 448–453.

140 E. Nolot, B. Caby, R. Gassilloud, M. Veillerot and D. Eichert, X-ray reflectometry and grazing-incidence X-ray fluorescence characterization of innovative electrodes for tantalum-based resistive random access memories, *Spectrochim. Acta, Part B*, 2018, **149**, 71–75. Available from: **https://www.sciencedirect.com/science/article/pii/S0584854718300569**.

141 M. A. Alam, M. K. Tiwari, A. Khooha, M. Nayak and C. Mukherjee, Structural characterization of Au/Cr bilayer thin films using combined X-ray reflectivity and grazing incidence X-ray fluorescence measurements, *Surf. Interface Anal.*, 2022, **54**(10), 1032–1040. Available from: **https://analyticalsciencejournals.onlinelibrary.wiley.com/doi/abs/10.1002/sia.7128**.

142 M. A. Rodriguez, T. F. Babuska, J. Curry, J. J. M. Griego, M. T. Dugger, S. R. Larson, *et al.*, Characterization of MoS2 films via simultaneous grazing incidence X-ray diffraction and grazing incidence X-ray fluorescence (GIXRD/GIXRF), *Powder Diffr.*, 2024, **39**(2), 60–68.

143 M. K. Tiwari, G. S. Lodha and K. J. S. Sawhney, Applications of the 'CATGIXRF' computer program to the grazing incidence X-ray fluorescence and X-ray reflectivity characterization of thin films and surfaces, *X-Ray Spectrom.*, 2010, **39**(2), 127–134. Available from: **https://analyticalsciencejournals.onlinelibrary.wiley.com/doi/abs/10.1002/xrs.1215**.

144 K. V. Nikolaev, A. I. Safonov, O. A. Kondratev, G. V. Prutskov, I. A. Likhachev, I. A. Subbotin, *et al.*, Grazing-emission X-ray fluorescence as a multiprobe tool for thin-film metrology, *J. Appl. Crystallogr.*, 2023, **56**(5), 1435–1445, DOI: **10.1107/S1600576723007112**.

145 C. de Mello Donegá, S. G. Hickey, S. F. Wuister, D. Vanmaekelbergh and A. Meijerink, Single-Step Synthesis to Control the Photoluminescence Quantum Yield and Size Dispersion of CdSe Nanocrystals, *J. Phys. Chem. B*, 2003, **107**(2), 489–496, DOI: **10.1021/jp027160c**.

146 J. B. Hannon, S. Kodambaka, F. M. Ross and R. M. Tromp, The influence of the surface migration of gold on the growth of silicon nanowires, *Nature*, 2006, **440**, 69–71, DOI: **10.1038/nature04574**.

147 J. M. Mativetsky, S. A. Burke, S. Fostner and P. Grutter, Nanoscale Pits as Templates for Building a Molecular Device, *Small*, 2007, **3**(5), 818–821, DOI: **10.1002/smll.200600699**.

148 M. Howarth, W. Liu, S. Puthenveetil, Y. Zheng, L. F. Marshall, M. M. Schmidt, *et al.*, Monovalent, reduced-size quantum dots for imaging receptors on living cells, *Nat. Methods*, 2008, **5**, 397–399. Available from: **http://www.nature.com/nmeth/journal/v5/n5/suppinfo/nmeth.1206_S1.html**.

149 M. K. Tiwari, G. M. Bhalerao, M. Babu, A. K. Sinha and C. Mukherjee, Investigation of metal nanoparticles on a Si surface using an x-ray standing wave field, *J. Appl. Phys.*, 2008, **103**(5), 054311.

150 A. von Bohlen, M. Krämer, C. Sternemann and M. Paulus, The influence of X-ray coherence length on TXRF and XSW and the characterization of nanoparticles observed under grazing incidence of X-rays, *J. Anal. At. Spectrom.*, 2009, **24**, 792–800.

151 M. K. Tiwari, K. J. S. Sawhney, T. L. Lee, S. G. Alcock and G. S. Lodha, Probing the average size of self-assembled metal nanoparticles using x-ray standing waves, *Phys. Rev. B: Condens. Matter Mater. Phys.*, 2009, **80**, 035434.

152 A. Zargham, T. Schmidt, J. I. Flege, M. Sauerbrey, R. Hildebrand, S. Röhe, *et al.*, On revealing the vertical structure of nanoparticle films with elemental resolution: A total external reflection X-ray standing waves study, *Nucl. Instrum. Methods B*, 2010, **268**(3), 325–328. X-ray Techniques for Advanced Materials, Nanostructures and

3390 | *J. Anal. At. Spectrom.*, 2025, **40**, 3368–3393

This journal is © The Royal Society of Chemistry 2025

Thin Films: from Laboratory Sources to Synchrotron Radiation. Available from: https://www.sciencedirect.com/science/article/pii/S0168583X09009963.

153 M. Brücher, M. Chakif, E. L. Gurevich and R. Hergenröder, Polydisperse NiTi nanoparticles investigated by X-ray standing waves and electron microscopy—A comparative study, *Spectrochim. Acta, Part B*, 2014, **98**(0), 60–64. Available from: http://www.sciencedirect.com/science/article/pii/S0584854714000810.

154 Y. Kayser, J. Sá and J. Szlachetko, Nanoparticle characterization by means of scanning free grazing emission X-ray fluorescence, *Nanoscale*, 2015, **7**(20), 9320–9330.

155 A. Singh, K. Luening, S. Brennan, T. Homma, N. Kubo, S. H. Nowak, *et al.*, Determination of copper nanoparticle size distributions with total reflection X-ray fluorescence spectroscopy, *J. Synchrotron Radiat.*, 2017, **24**, 283–287.

156 R. Unterumsberger, P. Hönicke, Y. Kayser, B. Pollakowski-Herrmann, S. Gholhaki, Q. Guo, *et al.*, Interaction of nanoparticle properties and X-ray analytical techniques, *J. Anal. At. Spectrom.*, 2020, **35**, 1022–1033, DOI: 10.1039/D0JA00049C.

157 A. Bekshaev and R. van Grieken, Interference technique in grazing-emission electron probe microanalysis of submicrometer particles, *Spectrochim. Acta, Part B*, 2001, **56**(5), 503–515.

158 U. E. A. Fittschen, M. Menzel, O. Scharf, M. Radtke, U. Reinholz, G. Buzanich, *et al.*, Observation of X-ray shadings in synchrotron radiation-total reflection X-ray fluorescence using a color X-ray camera, *Spectrochim. Acta, Part B*, 2014, **99**, 179–184. Available from: https://www.sciencedirect.com/science/article/pii/S0584854714001293.

159 F. Reinhardt, J. Osan, S. Torok, A. E. Pap, M. Kolbe and B. Beckhoff, Reference-free quantification of particle-like surface contaminations by grazing incidence X-ray fluorescence analysis, *J. Anal. At. Spectrom.*, 2012, **27**, 248–255, DOI: 10.1039/C2JA10286B.

160 Z. M. Spolnik, M. Claes, R. E. Van Grieken, P. K. de Bokx and H. P. Urbach, Quantification in grazing-emission X-ray fluorescence spectrometry, *Spectrochim. Acta, Part B*, 1999, **54**(10), 1525–1537. Available from: http://www.sciencedirect.com/science/article/B6THN-3XNK82P-N/2/5b25da0a08028dec89cb05234c81e9ca.

161 A. Kuczumow, M. Schmeling and R. Van Grieken, Critical assessment and proposal for reconstruction of a grazing emission X-ray fluorescence instrument, *J. Anal. At. Spectrom.*, 2000, **15**, 535–542, DOI: 10.1039/A908661G.

162 D. Hellin, A. Delabie, R. L. Puurunen, P. Beaven, T. Conard, B. Brijs, *et al.*, Grazing Incidence-X-ray Fluorescence Spectrometry for the Compositional Analysis of Nanometer-Thin High-k Dielectric HfO2 Layers, *Anal. Sci.*, 2005, **21**, 845, DOI: 10.2116/analsci.21.845.

163 R. Klockenkämper and A. von Bohlen, Determination of the critical thickness and the sensitivity for thin-film analysis by total reflection X-ray fluorescence spectrometry, *Spectrochim. Acta, Part B*, 1989, **44**(5), 461–469. Available

from: http://www.sciencedirect.com/science/article/pii/0584854789800515.

164 M. Dialameh, F. Ferrarese Lupi, P. Hönicke, Y. Kayser, B. Beckhoff, T. Weimann, *et al.*, Development and Synchrotron-Based Characterization of Al and Cr Nanostructures as Potential Calibration Samples for 3D Analytical Techniques, *Phys. Status Solidi*, 2018, **215**(6), 1700866. Available from: https://onlinelibrary.wiley.com/doi/abs/10.1002/pssa.201700866.

165 S. W. King, H. Simka, D. Herr, H. Akinaga and M. Garner, Research Updates: The three M's (materials, metrology, and modeling) together pave the path to future nanoelectronic technologies, *APL Mater.*, 2013, **1**(4), 040701, DOI: 10.1063/1.4822437.

166 P. Pellacani, V. Torres-Costa, F. Agulló-Rueda, R. Vanna, C. Morasso and M. Manso Silván, Laser writing of nanostructured silicon arrays for the SERS detection of biomolecules with inhibited oxidation, *Colloids Surf. B Biointerfaces*, 2019, **174**, 174–180. Available from: https://www.sciencedirect.com/science/article/pii/S0927776518307860.

167 R. A. Pala, J. S. Q. Liu, E. S. Barnard, D. Askarov, E. C. Garnett, S. Fan, *et al.*, Optimization of non-periodic plasmonic light-trapping layers for thin-film solar cells, *Nat. Commun.*, 2013, **4**, 2095.

168 M. Malerba, A. Alabastri, E. Miele, P. Zilio, M. Patrini, D. Bajoni, *et al.*, 3D vertical nanostructures for enhanced infrared plasmonics, *Sci. Rep.*, 2015, **5**(1), 16436, DOI: 10.1038/srep16436.

169 A. Andrle, P. Hönicke, G. Gwalt, P. I. Schneider, Y. Kayser, F. Siewert, *et al.*, Shape- and Element-Sensitive Reconstruction of Periodic Nanostructures with Grazing Incidence X-ray Fluorescence Analysis and Machine Learning, *Nanomaterials*, 2021, **11**(7), 1647.

170 K. Matveevskii, K. V. Nikolaev, R. Fallica, D. Beckers, M. Gateshki, A. Kharchenko, *et al.*, Laboratory-based 3D X-ray standing-wave analysis of nanometre-scale gratings, *J. Appl. Crystallogr.*, 2024, **57**(5), 1288–1298.

171 S. Staeck, J. Baumann, P. Hönicke, N. A. Wauschkuhn, F. Spikermann, D. Grötzsch, *et al.*, Investigation of Ti nanostructures via laboratory scanning-free GEXRF, *Nanoscale*, 2025, **17**(6), 3411–3420.

172 L. M. Lohr, R. Ciesielski, V. B. Truong and V. Soltwisch, Hybrid approach to reconstruct nanoscale grating dimensions using scattering and fluorescence with soft X-rays, *Nanoscale*, 2025, **17**, 6017–6029, DOI: 10.1039/D4NR04580G.

173 N. Wauschkuhn, Y. Kayser, J. Baumann, J. Degenhardt, T. Siefke, V. B. Truong, *et al.*, Characterization and discrimination of periodic nanostructures with scanning-free GEXRF, *Nanotechnology*, 2025, **36**(23), 235701.

174 V. Truong, A. F. Herrero, K. Andrle, V. Soltwisch and P. Hönicke, Machine Learning-Accelerated Reconstruction of Periodic Nanostructures with X-ray Fluorescence Spectroscopy Methods, *Adv. Mater. Interfaces*, 2025, **12**(10), 2400898.

This journal is © The Royal Society of Chemistry 2025

J. Anal. At. Spectrom., 2025, **40**, 3368–3393 | **3391**

175 K. V. Nikolaev, V. Soltwisch, P. Hönicke, F. Scholze, J. de la Rie, S. N. Yakunin, *et al.*, A semi-analytical approach for the characterization of ordered 3D nanostructures using grazing-incidence X-ray fluorescence, *J. Synchrotron Radiat.*, 2020, **27**(2), 386–395, DOI: **10.1107/S1600577519016345**.

176 K. V. Nikolaev, V. Soltwisch, M. A. Botchev, A. F. Herrero, P. Hönicke, F. Scholze, *et al.*, Polygon-based unified Fourier-modal approach for diffractive-optics simulations, *Phys. Rev. A*, 2025 Sep;p.–. Available from: **https://link.aps.org/doi/10.1103/n2qj-l886**.

177 G. Pepponi, D. Giubertoni, M. Bersani, F. Meirer, D. Ingerle, G. Steinhauser, *et al.*, Grazing incidence x-ray fluorescence and secondary ion mass spectrometry combined approach for the characterization of ultrashallow arsenic distribution in silicon, *J. Vac. Sci. Technol. B*, 2010, **28**(1), C1C59–C1C64. Available from: **http://link.aip.org/link/?JVB/28/C1C59/1**.

178 P. Rajput, A. Gupta, S. Rajagopalan and A. K. Tyagi, Fe diffusion in amorphous Si studied using x-ray standing wave technique, *AIP Adv.*, 2012, **2**(1), 012159, DOI: **10.1063/1.3693403**.

179 Y. Kayser, D. Banaś, W. Cao, J. C. Dousse, J. Hoszowska, P. Jagodziński, *et al.*, Depth profiling of dopants implanted in Si using the synchrotron radiation based high-resolution grazing emission technique, *X-Ray Spectrom.*, 2012, **41**(2), 98–104, DOI: **10.1002/xrs.2372**.

180 P. Hönicke, M. Müller and B. Beckhoff, X-Ray induced depth profiling of ion implantations into various semiconductor materials, *Solid State Phenom.*, 2013, **195**, 274–276.

181 M. Kokkoris, E. G. Androulakaki, M. Czyzycki, M. Erich, A. G. Karydas, J. J. Leani, *et al.*, Argon ions deeply implanted in silicon studied by Rutherford/Elastic Backscattering and Grazing Incidence X-ray Fluorescence spectroscopy, *Nucl. Instrum. Methods Phys. Res., Sect. B*, 2019, **450**, 144–148.

182 M. Czyzycki, M. Kokkoris and A. G. Karydas, A mathematical model for deep ion implantation depth profiling by synchrotron radiation grazing-incidence X-ray fluorescence spectrometry, *J. Anal. At. Spectrom.*, 2020, **35**(12), 2964–2973.

183 M. A. Alam, M. K. Tiwari, D. Devi, S. Tripathi, A. Trivedi, S. Ojha, *et al.*, Depth profile analysis of 100 keV Ni ions in Si ⟨100⟩ substrate, *Spectrochim. Acta, Part B*, 2023, **206**, 106707. Available from: **https://www.sciencedirect.com/science/article/pii/S0584854723000940**.

184 J. F. Ziegler, M. D. Ziegler and J. P. Biersack, SRIM – The stopping and range of ions in matter (2010), *Nucl Inst Meth B.*, 2010, **268**(11–12), 1818–1823.

185 S. M. P. Smolders and H. P. Urbach, On the determination of dopant-concentration profiles by grazing emission X-ray fluorescence spectroscopy using the maximum-entropy method, *J. Eng. Math.*, 2002, **43**(2/4), 115–134.

186 A. Okhrimovskyy and K. Tsuji, Numerical approach for depth profiling with GE-XRF, *X-Ray Spectrom.*, 2006, **35**(5),

305–311. Available from: **https://onlinelibrary.wiley.com/doi/abs/10.1002/xrs.912**.

187 B. Pollakowski, B. Beckhoff, F. Reinhardt, S. Braun and P. Gawlitza, Speciation of deeply buried TiO_x nanolayers with grazing-incidence X-ray fluorescence combined with a near-edge X-ray absorption fine-structure investigation, *Phys. Rev. B: Condens. Matter Mater. Phys.*, 2008, **77**(23), 235408.

188 B. Pollakowski, P. Hoffmann, M. Kosinova, O. Baake, V. Trunova, R. Unterumsberger, *et al.*, Nondestructive and Nonpreparative Chemical Nanometrology of Internal Material Interfaces at Tunable High Information Depths, *Anal. Chem.*, 2013, **85**(1), 193–200, DOI: **10.1021/ac3024872**.

189 R. Fox and S. J. Gurman, EXAFS and surface EXAFS from measurements of X-ray reflectivity, *J. Phys. C Solid State Phys.*, 1980, **13**(11), L249. Available from: **http://stacks.iop.org/0022-3719/13/i=11/a=002**.

190 Y. Suzuki, Surface extended X-ray-absorption fine-structure spectroscopy measurement using the evanescent-wave effect of fluorescent X-ray, *Phys. Rev. B: Condens. Matter Mater. Phys.*, 1989, **39**(5), 3393–3395.

191 L. Tröger, D. Arvanitis, K. Baberschke, H. Michaelis, U. Grimm and E. Zschech, Full correction of the self-absorption in soft-fluorescence extended x-ray-absorption fine structure, *Phys. Rev. B: Condens. Matter Mater. Phys.*, 1992, **46**, 3283–3289. Available from: **http://link.aps.org/doi/10.1103/PhysRevB.46.3283**.

192 P. Pfalzer, J. P. Urbach, M. Klemm, S. Horn, M. L. denBoer, A. I. Frenkel, *et al.*, Elimination of self-absorption in fluorescence hard-x-ray absorption spectra, *Phys. Rev. B: Condens. Matter Mater. Phys.*, 1999, **60**, 9335–9339. Available from: **http://link.aps.org/doi/10.1103/PhysRevB.60.9335**.

193 Y. Kayser, J. Sá and J. Szlachetko, Depth-Resolved X-ray Absorption Spectroscopy by Means of Grazing Emission X-ray Fluorescence, *Anal. Chem.*, 2015, **87**(21), 10815–10821.

194 M. Sakamaki and K. Amemiya, Nanometer-resolution depth-resolved measurement of fluorescence-yield soft x-ray absorption spectroscopy for FeCo thin film, *Rev. Sci. Instrum.*, 2017, **88**(8), 083901, DOI: **10.1063/1.4986146**.

195 M. Sakamaki and K. Amemiya, Observation of an electric field-induced interface redox reaction and magnetic modification in GdOx/Co thin film by means of depth-resolved X-ray absorption spectroscopy, *Phys. Chem. Chem. Phys.*, 2018, **20**, 20004–20009, DOI: **10.1039/C8CP02972E**.

196 K. Shinoda, S. Suzuki, K. Yashiro, J. Mizusaki, T. Uruga, H. Tanida, *et al.*, Nondestructive depth-resolved chemical state analysis of (La,Sr)MnO3 film under high temperature, *Surf. Interface Anal.*, 2010, **42**(10–11), 1650–1654.

197 T. Okumura, T. Nakatsutsumi, T. Ina, Y. Orikasa, H. Arai, T. Fukutsuka, *et al.*, Depth-resolved X-ray absorption spectroscopic study on nanoscale observation of the electrode-solid electrolyte interface for all solid state lithium ion batteries, *J. Mater. Chem.*, 2011, **21**(27), 10051–10060, DOI: **10.1039/C0JM04366D**.

3392 | *J. Anal. At. Spectrom.*, 2025, **40**, 3368–3393

This journal is © The Royal Society of Chemistry 2025

198 D. Takamatsu, T. Nakatsutsumi, S. Mori, Y. Orikasa, M. Mogi, H. Yamashige, *et al.*, Numerical approach for depth profiling with GE-XRF, *J. Phys. Chem. Lett.*, 2011, **2**(20), 2511–2514, DOI: **10.1021/jz2011226**.

199 K. Beppu, S. Yamazoe, A. Yamada, K. Nitta, T. Uruga and T. Wada, Structural analysis of Cu(In,Ga)Se2 thin-films by depth-resolved XAFS, *Jpn. J. Appl. Phys.*, 2019, **58**(10), 105502, DOI: **10.7567/1347-4065/ab4573**.

200 K. Sakata and K. Amemiya, Time- and Depth-Resolved Chemical State Analysis of the Surface-to-Subsurface Oxidation of Cu by X-ray Absorption Spectroscopy at Near Ambient Pressure, *J. Phys. Chem. Lett.*, 2022, **13**(41), 9573–9580, DOI: **10.1021/acs.jpclett.2c02641**.

201 A. Kubala-Kukuś, D. Banaś, W. Cao, J. C. Dousse, J. Hoszowska, Y. Kayser, *et al.*, Observation of ultralow-level Al impurities on a silicon surface by high-resolution grazing emission X-ray fluorescence excited by synchrotron radiation, *Phys. Rev. B: Condens. Matter Mater. Phys.*, 2009, **80**(11), 113305.

202 Y. Kayser, J. Osán, P. Hönicke and B. Beckhoff, Reliable compositional analysis of airborne particulate matter beyond the quantification limits of total reflection X-ray fluorescence, *Anal. Chim. Acta*, 2022, **1192**, 339367. Available from: **https://www.sciencedirect.com/science/article/pii/S0003267021011934**.

This journal is © The Royal Society of Chemistry 2025

J. Anal. At. Spectrom., 2025, **40**, 3368–3393 | **3393**